Encyclopaedia of Fluid Mechanics, □
Ed. N. P. Cheremisinoff, □
Gulf Publishing Company, Houston, Texas, □
Vol. 6 (1987) p. 1337-1391

CHAPTER 34

DIRECT NUMERICAL AND LARGE EDDY SIMULATION OF TURBULENT CHANNEL FLOWS

Günther Grötzbach

Kernforschungszentrum Karlsruhe
Institut für Reaktorentwicklung
Karlsruhe, Federal Republic of Germany

CONTENTS

INTRODUCTION

Technical and natural fluid flow and convective heat transfer problems are in general in the parameter range of turbulent flows. In this context turbulence means a three-dimensional time-dependent motion in which vortex stretching causes velocity fluctuations. The small eddies are determined by viscous forces and the large eddies by the special boundary conditions. Thus the features of turbulence strongly depend on the type of flow considered.

Often details of turbulence are not of interest for practical purposes, and so the methods widely used for numerical investigations are based on the so-called Reynolds equations. That means the conservation equations for mass, momentum, and energy are averaged over time intervals which are relevant for turbulence effects. Due to this time-averaging procedure unknown turbulent shear stresses and heat fluxes appear in these equations. Models must be introduced like the eddy diffusivity models which have to represent the total information on the effects of turbulence. Due to the features of turbulence such Reynolds models may only be used as an interpolative tool for those types of flows for which the model coefficients have been calibrated. So these models cannot be used universally, but they do an excellent and efficient job in case of adequate applications.

When such restrictions shall be avoided the complete Navier-Stokes equations must be solved. Evidently there are no adjustable model parameters in this case and therefore this direct simulation should be universal. As the size of the smallest eddies decrease with increasing Reynolds numbers

but must be resolved in the calculation, direct simulations are restricted to low Reynolds numbers even when the largest and fastest available computers are used. In large Reynolds number flows one can only resolve the large turbulence scales of the flow. The small eddies not resolvable by the method have to be accounted for by subgrid scale models. Such so-called large eddy simulations profit from the fact that the large scales which determine the characteristics of the individual flow are directly simulated. The small scales which have to be modeled are known to obey more or less universal laws. Therefore large eddy simulation is a fairly universal method.

The objectives of this paper are to give an introduction to the methods of direct and large eddy simulations, and to give some typical examples. Starting from a volume integration formalism a finite difference scheme will be deduced for the conservation equations which has some advantage in handling strongly anisotropic grids. An appropriate subgrid scale model will be introduced including viscous and conductive effects in the wall region. The coefficients used in the model will be determined from the spectral theory for isotropic turbulence. So there is an automatic and continuous transition from a direct simulation to a large eddy simulation depending on local flow and grid parameters. A short discussion of the space and time integration scheme will be followed by that of the important topic of boundary conditions, and the less crucial problem of initial conditions.

Three examples will be given for different types of flows. Each presentation will start from a check on whether the spatial resolution requirements for direct numerical simulations will be met by grids tolerable on available computer systems. The first example, an internally heated convection layer, can be treated by direct numerical simulation up to the fully turbulent regime. The second example, the pressure-driven flow of liquid metals, can be treated by a mixed simulation: At low Peclet numbers the temperature field can be simulated directly, whereas the velocity field has to be described by a large eddy simulation model. The third example, a pressure-driven flow with initially strong buoyancy forces, can only be handled by a large eddy simulation scheme. The rough grid chosen for this prototypical engineering problem clearly shows that large eddy simulations do not necessarily consume immense amounts of computing time.

The Methods of Direct Numerical and Large Eddy Simulation

Three main requirements for any direct numerical simulation model can be deduced following the definition of turbulence given in the introduction: The numerical model must record all relevant scales, from the largest scales of eddies dominated by the bounding geometry to the smallest scales dominated by the viscous forces. Therefore the model has to include all viscous terms. It must also include the nonlinear convective terms because vortex interaction is a nonlinear mechanism. Furthermore the model must be time dependent and three dimensional. This simply means that any direct simulation method for turbulent flows must use the complete conservation equations and a numerical discretization which is appropriate to all important scales of the flow.

The spectral method is one of the available numerical procedures to integrate nonlinear partial differential equations. The dependent variables in the conservation equations are expanded in Fourier or Chebyshev series or in any terms of other sets of globally smooth functions. This method has been expected to be much more accurate than finite difference schemes. Thus the main field of application is the investigation of the instabilities leading to the transition from laminar to turbulent flow. The method has been used, e.g., by Orszag and his coworkers [1, 2] and by Kleiser [3, 4] for studies of the transition in Poiseuille flow, and by McLaughlin and Orszag [5] for the transition in Bénard convection. Numerical tests by Schumann et. al. [6] with spectral schemes and finite difference schemes on suitable nonequidistant grids have shown that only at very large mode numbers the accuracy of spectral schemes is better than that of a second-order finite difference scheme. Thus the spectral simulations are particularly suited if extremely high accuracy is required as in laminar to turbulent transition simulations. Introductions to direct numerical simulation by spectral methods have been given, e.g., by Orszag and Israeli [7], by Orszag [8], and by Schumann et al. [6].

Another available method to numerically integrate the conservation equations uses finite difference schemes. The partial derivatives of the dependent variables are approximated by finite differences for the local volume-averaged variables. The main advantages of finite difference methods

in comparison to spectral methods are their simplicity and flexibility with respect to boundary conditions. The finite difference method is usually applied to large eddy simulations of high Reynolds number flows, but is also often applied to direct simulations of transition flow problems. Introductions to large eddy simulations based on finite difference schemes and critical reviews of important applications have been given, e.g., by Love [9], Chapman [10], Schumann et al. [6], Ferziger [11], and Leslie [12]. Here the volume-averaging procedure used by Schumann [13] will be applied to formally deduce a finite difference scheme for the basic equations and to identify the meaning of the subgrid scale terms.

Basic Conservation Equations

The basic equations for laminar and turbulent convection with heat transfer are the conservation equations for mass, momentum, and energy. For the sake of simplicity the Boussinesq approximation is adopted. This implies the assumption that the physical properties in all terms of these equations can be considered as constant except for the buoyancy term. If Cartesian coordinates (x_1, x_2, x_3) are used for plane channels with the mean flow direction x_1 and x_3 directed perpendicular to the walls, then the equations for the velocity components u_i (i = 1, 2, 3), pressure p, and temperature T are:

$$\frac{\partial u_i}{\partial x_i} = 0 \tag{1a}$$

$$\frac{\partial u_i}{\partial t} + \frac{\partial u_i u_j}{\partial x_j} = \frac{\partial}{\partial x_j}\left(\frac{1}{Re_0}\frac{\partial u_i}{\partial x_j}\right) - \frac{\partial p}{\partial x_i} + P_z\delta_{1i} - \frac{Ra}{Re_0^2 Pr}(T_{ref} - T)\delta_{ik} \tag{1b}$$

$$\frac{\partial T}{\partial t} + \frac{\partial T u_j}{\partial x_j} = \frac{\partial}{\partial x_j}\left(\frac{1}{Re_0 Pr}\frac{\partial T}{\partial x_j}\right) + \dot{Q} \tag{1c}$$

The Einstein summation rule is applied to all terms bearing the same subscript twice. In the buoyancy term the subscript k denotes the direction opposite to the gravity vector. The mean pressure gradient or driving force P_z is introduced so that the fluctuating pressure field p has a zero mean gradient in the x_1-direction.

Equations 1 are normalized with the plate spacing $\hat{D}$ (variables marked by $\hat{}$ are dimensional), the time scale $\hat{t} = \hat{D}/\hat{u}_0$, and the pressure $\hat{p} = \hat{\rho}\hat{u}_0^2$, where $\hat{\rho}$ is the density. Thus the dimensionless numbers used are the Reynolds number, $Re_0 = (\hat{u}_0\hat{D})/\hat{\nu}$, the Prandtl number, $Pr = \hat{\nu}/\hat{a}$, and the Rayleigh number, $Ra = \hat{g}\hat{\beta}\hat{Q}\hat{D}^5/(\hat{\nu}\hat{a}\hat{\lambda})$

where $\hat{g}$ = gravity
$\hat{\beta}$ = volume expansion coefficient
$\hat{\nu}$ = kinematic viscosity
$\hat{a}$ = temperature conductivity coefficient

The homogeneously distributed internal heat source $\dot{Q}$ within the fluid can be rewritten as $\dot{Q} = Da_0/(Re_0 Pr)$, where $Da_0 = \hat{Q}\hat{D}^2/(\hat{\lambda}\hat{T}_0)$ is the Damköhler number and $\hat{\lambda}$ = thermal conductivity.

The velocity scale $\hat{u}_0$ and temperature scale $\hat{T}_0$ can freely be chosen. There are, however, two practical restrictions. The first concerns an easy readability and understanding of the numerical results, and the second is due to accuracy considerations: The calculated velocities and temperatures should be of about the same order of magnitude in order to minimize truncation errors. These requirements are met by choosing $\hat{u}_0 = (\hat{\tau}_0/\hat{\rho})^{1/2}$ = friction velocity and $\hat{T}_0 = \hat{q}_0/(\hat{\rho}\hat{C}_p\hat{u}_0)$ = heat-flux temperature for pressure driven flows

where $\hat{\tau}_0$ = time mean wall shear stress averaged over both walls
$\hat{q}_0$ = time mean wall heat flux
$\hat{C}_p$ = specific heat capacity

For symmetrical boundary conditions this directly gives the numerical results in units of u^+ and T^+. The resulting driving force is $P_z = 2$ and the internal heat source $\dot{Q} = 2$, or $\dot{Q} = 1$ in case of one adiabatic wall. The common Reynolds number $Re = \hat{u}_b 2\hat{D}/\hat{\nu}$ based on the bulk velocity $\hat{u}_b$ and the friction coefficient C_f are related to Re_0 by:

$$Re_0 = Re\ \hat{u}_0/(2\hat{u}_b) = Re(C_f/32)^{1/2} \tag{2}$$

The scales used for pure natural convection of internally heated horizontal fluid layers with isothermal walls are $\hat{u}_0 = (\hat{g}\hat{\beta}\hat{T}_0\hat{D})^{1/2}$ and $\hat{T}_0 = \hat{T}_{max} - \hat{T}_w$. The difference between the maximum time mean temperature and the mean wall temperature is calculated using the dependence between the Damköhler and Nusselt numbers at the lower and the upper wall, Nu_1 and Nu_2, respectively:

$$Da_0 = Nu_1 + Nu_2 \tag{3}$$

The reference temperature T_{ref} in the buoyancy term must in any case be chosen to be appropriate to the problem. In most flow problems, especially in natural convection in horizontal fluid layers, T_{ref} must be set equal to the volume average in the entire channel, ${}^v\langle T\rangle$, in order to avoid a net contribution of the buoyancy term to the pressure.

Volume-Averaged Equations

The first step in the deduction of a finite difference scheme for the basic conservation equations is to define the variables which will be treated by such a scheme. On a given finite difference grid only the fluctuations of flow variables having wavelengths larger than a few grid widths will be directly resolved. Shorter wavelengths cannot be resolved and have to be modeled. Thus one has to introduce a formalism which splits the physical variables into the directly resolved parts and in the unresolved, the so-called subgrid scale parts.

For practical simulations three different splitting formalisms have been used: Smagorinsky [14] and Lilly [15] assumed that the resolved flow field variables may be defined by linear volume averages over the mesh cell volumes and that therefore the smallest resolvable wavelength is two times the grid width. This formalism replaces the basic Equations 1 by a set of partial differential equations for the volume averaged variables. It has been used, e.g., by Deardorff [16, 17] and Schemm and Lipps [18]. The second formalism introduced by Schumann [13, 19] starts from the same assumptions. In integrating the basic Equations 1 by parts, most partial derivatives are formally replaced by finite difference operators. As a result one gets a nearly directly programmable finite difference scheme for mesh cell volume and surface averaged variables. This method has been used by Schumann [13, 20] and the author [21, 22]. The third formalism introduced by Leonard [23] uses nonlinear weighting functions for filtering out the fine-scale motion. The filtered basic equations are still partial differential equations. In contrast to all other methods these equations contain additional unknown filtered interactions of filtered velocities, the so-called Leonard stresses. The method has been extensively used by the Stanford group, e.g., by Mansour et al. [24] and by Moin et al. [25].

Here, the second procedure is used to deduce conservation equations for the resolvable fluctuations of the flow field. Following Schumann [13] the basic Equations 1 are formally integrated over a mesh cell volume, $v = \Delta x_1\,\Delta x_2\,\Delta x_3$. This furnishes the volumetric average for any variable y:

$${}^v\bar{y} = \frac{1}{\Delta x_1\,\Delta x_2\,\Delta x_3}\int_{\Delta x_1}\int_{\Delta x_2}\int_{\Delta x_3} y(x_1', x_2', x_3')\,dx_3'\,dx_2'\,dx_1' \tag{4}$$

By applying Gauss's theorem the volume average of the partial derivatives is transformed into a finite-difference form of the surface average values ${}^i\bar{y}$, where i denotes the index of the direction normal to the respective mesh cell surface ${}^iF = v/\Delta x_i$:

$$\overline{{}^v\frac{\partial y}{\partial x_i}} = \frac{1}{\Delta x_i}\left[{}^i\bar{y}\left(x_i + \frac{\Delta x_i}{2}\right) - {}^i\bar{y}\left(x_i - \frac{\Delta x_i}{2}\right)\right] = \delta_i\,{}^i\bar{y} \tag{5}$$

Application of Operators 4 and 5 to the basic conservation Equations 1a-c provides the following finite difference formulae:

$$\delta_i\,{}^i\bar{u}_i = 0 \qquad i = 1, 2, 3 \tag{6a}$$

$$\frac{\partial {}^v\bar{u}_i}{\partial t} + \delta_j\,\overline{{}^iu_i{}^ju_j} = \delta_j\left(\frac{1}{Re_0}\overline{{}^j\frac{\partial u_i}{\partial x_j}}\right) - \delta_i\,{}^i\bar{p} + {}^v\bar{P}_z\delta_{i1} - \frac{Ra}{Re_0^2 Pr}\,\Delta\,{}^v\bar{T}\delta_{ik} \tag{6b}$$

$$\frac{\partial {}^v\bar{T}}{\partial t} + \delta_j\,\overline{{}^ju_jT} = \delta_j\left(\frac{1}{Re_0 Pr}\overline{{}^j\frac{\partial T}{\partial x_j}}\right) + {}^v\bar{Q} \tag{6c}$$

The averaged nonlinear terms can be rewritten using the definitions implied by the volume-averaging procedure. The Operator 4 splits velocity and temperature fields into spatial averages, ${}^j\bar{u}_j$, ${}^v\bar{T}$, with typical wavelengths larger than Δx_i, which are directly resolved by the grid, and into "subgrid scale" parts, $u_j' = u_j - {}^j\bar{u}_j$, $T' = T - {}^v\bar{T}$, with wavelengths smaller than Δx_i, which are not spatially resolved. Thus one gets:

$$\overline{{}^iu_i{}^ju_j} = {}^i\bar{u}_i\,{}^j\bar{u}_j + \overline{{}^iu_i'u_j'} \tag{7a}$$

$$\overline{{}^ju_jT} = {}^j\bar{u}_j\,{}^j\bar{T} + \overline{{}^ju_j'T'} \tag{7b}$$

The first terms on the right-hand side represent the resolvable part of the instantaneous turbulent shear stresses and heat fluxes, the second terms represent the unresolved subgrid scale parts which have to be modeled. In contrast to Smagorinsky's volume-averaging procedure the subgrid scale terms are not averaged over mesh cell volumes but over single surfaces of mesh cells. This has important advantages in case of handling highly anisotropic grids [13, 21]. In contrast to Leonard's filtering procedure, no Leonard terms, that means no additional averaged cross-products between grid scale and subgrid scale variables exist because the filter function, Equation 4, used here is linear. Some results by Antonopoulos-Domis [26] and discussions given by Schumann et al. [6] and Leslie [12] seem to confirm that Schumann's volume-averaging procedure is not only the simpler method to define the calculated and unknown variables but that it also gives the more realistic numerical results.

Subgrid Scale Models

Equations 6 and 7 look like the Reynolds equations deduced by time averaging. In the Reynolds equations, models must be introduced for the unknown shear stresses which contain all information on turbulence independent of the actual spatial discretization. Here, Equations 6 and 7 are, however, not averaged over time, but over the mesh cell volumes only. Therefore, the unknown terms $\overline{{}^iu_i'u_j'}$ and $\overline{{}^ju_j'T'}$ contain only the small-scale information on turbulence, which cannot be spatially resolved by the grid. This kind of method is called large eddy simulation. The subgrid scale terms tend to zero if one uses highly resolving grids. In such direct numerical simulations the subgrid scale terms are of no physical importance, but formally the terms still appear in the averaged conservation equations. This holds even for laminar flows. (Similar subgrid scale terms should also appear in the finite difference form of the Reynolds equations in addition to the unknown shear stresses but are usually neglected. The physical meaning and importance of these terms is similar and depends also on the spatial discretization, but it strongly depends in addition on the flow problem considered).

The physical relevance of the subgrid scale terms in large eddy simulations of high Reynolds number flows can be explained by discussing the behavior of turbulence in wave-number space, e.g., its spectral distribution as given in Figure 1. Most kinetic energy is associated with large

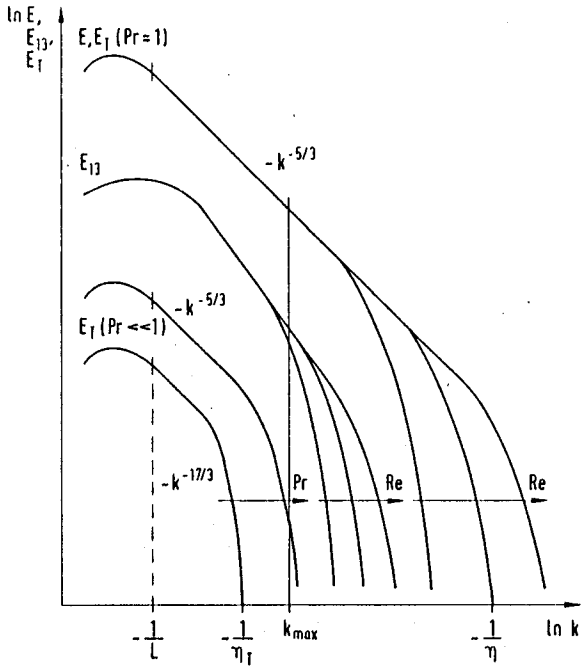

Figure 1. Spectra of the tubulent fluctuations of kinetic energy E, turbulent shear stress E_{13}, and temperature E_T vs. wave-number k for different Reynolds and Prandtl numbers. k_{max} is the resolution barrier of a finite difference grid.

wavelengths around L, where L is a typical macroscopic length scale of the flow, as for example, the channel width. This is the range where turbulence is directly produced by instabilities of the mean flow. The motion of the large eddies is again unstable and results in smaller and ever smaller eddies. After many such cascade processes the length scales of the eddies are no longer related to the largest scales. They solely depend on the viscosity and the amount of the energy flux coming from the large scales resulting finally at small scales in the dissipation ε. The intermediate range in the energy spectrum can be described by the Kolmogorov spectrum:

$$E(k) = \alpha \varepsilon^{2/3} k^{-5/3} \tag{8}$$

The coefficient α seems to be independent of the type of flow. Its value is between 1.5 and 1.6 [21, 27]. The one-way street of energy ends at small scales, where the kinetic turbulence energy is dissipated by viscous forces at length scales around:

$$\eta = (\nu^3/\varepsilon)^{1/4} \tag{9}$$

The spectrum of the turbulent shear stress, E_{13}, is steeper than that of the kinetic energy. Therefore, the smallest eddies carry only energy, but no turbulent shear forces. In this small scale or high wave-number range the velocity field is locally isotropic. Thus, the mathematical tools for isotropic turbulence as summarized, e.g., by Hinze [28] and Monin and Yaglom [29] can be applied to determine the model coefficients. The spectra of temperature fluctuations are analogous to those of the velocity fluctuations and can be described by the Batchelor spectrum:

$$E_T(k) = \beta \varepsilon^{-1/3} \varepsilon_T k^{-5/3} \tag{10}$$

Here ε_T = the dissipation of temperature variances
β = an empirical coefficient for which the data scatter between 0.2 and 1.8 [21].

The high wave-number cutoff is at length scales around:

$$\eta_T = (a^3/\varepsilon)^{1/4} \tag{11}$$

Here again mathematical tools are available, e.g. in [28, 29], to describe the statistics of isotropic temperature fluctuations. These tools can be used to determine the coefficients of the subgrid scale heat flux model.

The resolution barrier k_{max} for a rather coarse grid is also shown in Figure 1. The large scales, or the low wave-number scales, are resolved; the small scales, or high wave-number scales, have to be modeled. The resolution barrier cuts the energy spectrum E within the Kolmogorov range. This has been verified by experimental data to be valid for most grids used up to now for large eddy simulations of channel flows with Reynolds numbers in the order of 10^5 [19, 30]. The resolution bound also cuts the shear stress spectrum. Therefore, at these Reynolds numbers the subgrid scales are not completely isotropic, but only in their highest wave-number parts. On the other hand the resolution bound does not cut the temperature spectrum for small Prandtl numbers. So combined large eddy simulations of the velocity field and direct simulations of the temperature field are possible for liquid metals at these Reynolds numbers [21, 31]. For all spectra one finds that the importance of the subgrid scale terms increases with increasing Reynolds or Prandtl numbers and, due to

$$k_{max} = \pi/\Delta x \tag{12}$$

also with increasing grid widths.

The subgrid scale assumptions used in large eddy simulations are mainly based on the formal analogy to known Reynolds-type models except that the characteristic macroscopic length scales in these models have been replaced by the grid width Δx, and the mean velocity scale by a subgrid scale velocity.

- There are algebraic eddy viscosity models like the one introduced by Smagorinsky [14]. The model is not completely universal because for most applications the model coefficient as calculated by Lilly [15] has to be adapted individually. A discussion of this problem is given in Reference 32.
- One finds also eddy viscosity models with one additional transport equation for the subgrid scale kinetic energy like the one by Schumann [13]. He split the subgrid scale parts into an isotropic and an inhomogeneous part. Therefore the theory of isotropic turbulence can be strictly applied to calculate the model coefficients depending on local grid parameters. The present author introduced the dependence of the coefficients on local flow variables which led to a more universal subgrid scale model [21, 31].
- There also exist higher order transport equation models as introduced by Deardorff [17] and Schemm and Lipps [18]. These require a large number of additional transport equations for subgrid scale quantities and thus these models cause an enormous numerical effort. It has been shown that even for meteorological problems no complete second-order moment approach is necessary [18].
- There also exist models which use only few transport equations for second-order moments and some additional algebraic relations for other higher-order moments. These models, e.g., those by Schemm and Lipps [18] and Sommeria [33], still require more empirical information to determine relevant coefficients than do the eddy viscosity models.

It has also been proposed to simply neglect the subgrid scale terms and to extrapolate instead the numerical results to zero grid size by the truncation error functions of the finite difference

scheme [34]. This procedure implies that the physical information included in the subgrid scale terms may be replaced by the truncation errors which are in any case inherent to the finite difference scheme. It becomes obvious from Figure 1 that the functional dependence of the subgrid scale terms with the grid widths changes with the steepness in the spectra. However, the truncation errors follow fixed relations. Therefore, such an extrapolation can only work in case of direct numerical simulations but not in large eddy simulations. Further practical problems of the extrapolation method will be raised later.

In the following sections the subgrid scale model as introduced by Schumann [13] and extended by the author [21, 35] will be presented.

Subgrid Scale Flux Assumptions

The discussion of the spectra has shown that the subgrid scale fluxes at high Reynolds numbers and far away from walls are locally isotropic only in the high wave-number range. In the low wave-number range the fine structure is nonisotropic and inhomogeneous near walls, and in fact already quite far from them. Therefore, the subgrid scale fluxes in Equations 7a and b are formally split into a so-called "locally isotropic" and an "inhomogeneous part." For both parts gradient diffusion is assumed:

$$ {}^{j}\overline{u_i'u_j'} = -{}^{ij}\mu(D_{ij} - \langle D_{ij}\rangle) - {}^{ij}\mu^*\langle D_{ij}\rangle \tag{13a} $$

$$ {}^{j}\overline{u_j'T'} = -{}^{j}a_t(D_{Tj} - \langle D_{Tj}\rangle) - {}^{j}a_t^*\langle D_{Tj}\rangle \tag{13b} $$

where

$$ D_{ij} = \partial u_i/\partial x_j + \partial u_j/\partial x_i \tag{14a} $$

$$ D_{Tj} = \partial T/\partial x_j \tag{14b} $$

The angular brackets denote time mean or ensemble averages. The unknown eddy diffusivities ${}^{ij}\mu$ and ${}^{ij}\mu^*$, and eddy conductivities ${}^{j}a_t$ and ${}^{j}a_t^*$ are calculated from modified common turbulence models:

The isotropic eddy diffusivities ${}^{ij}\mu$ are determined by a Prandtl-energy-length-scale-type model. The isotropic eddy conductivities ${}^{j}a_t$ are modeled in an analogous manner, assuming that the subgrid scale heat flux depends on the velocity fluctuations within the grid cells:

$$ {}^{ij}\mu = C_2\,{}^{ij}C({}^{j}F{}^{j}C_5\,{}^{v}\overline{E'})^{1/2} \tag{15a} $$

$$ {}^{j}a_t = C_{T2}\,{}^{j}C_T({}^{j}F{}^{j}C_5\,{}^{v}\overline{E'})^{1/2} \tag{15b} $$

Here, the characteristic length scale, ${}^{j}F^{1/2}$, is taken from the surface area over which the averaged quantities in Equations 13 are defined. The characteristic velocity scale, ${}^{v}\overline{E'}^{1/2}$, is taken from the subgrid scale kinetic energy. Both scales go to zero if the grid width tends to zero.

The coefficients ${}^{ij}C$ and ${}^{j}C_T$ account for the anisotropies introduced by the finite difference scheme, which arise on anisotropic grids with $\Delta x_1 \neq \Delta x_2 \neq \Delta x_3$. But they also arise on isotropic grids because derivatives of $\partial u_1/\partial x_1$ and $\partial u_1/\partial x_2$, for example, require different finite difference forms in the grid, as can be seen from Equation 16c.

$$ {}^{ij}C = \frac{\langle {}_3\bar{D}_{ij}^2\rangle}{\langle {}_3\bar{D}_{(ij)(ij)}^2\rangle}\cdot\frac{\langle D_{(ij)(ij)}^2\rangle}{\langle D_{ij}^2\rangle} \tag{16a} $$

$$ {}^{j}C_T = \frac{\langle {}_1\bar{D}_{Tj}^2\rangle}{\langle {}_1\bar{D}_{T(j)}^2\rangle}\cdot\frac{\langle D_{T(j)}^2\rangle}{\langle D_{Tj}^2\rangle} \tag{16b} $$

where

$$ {}_3\overline{D_{ij}}^2 = 2\delta_{ij}(\delta_j\,{}^{j}\bar{u}_i)^2 + 1/2(1-\delta_{ij})\overline{(\delta_i\,{}^{j}\bar{u}_j + \delta_j\,{}^{i}\bar{u}_i)^2}^{j} \tag{16c} $$

$$ {}_1\overline{D_{1j}}^2 = (\delta_j\,{}^{j}\bar{T})^2 \tag{16d} $$

The overbar —j denotes linear averaging over two neighboring values in the j direction. (Einstein's summation rule must not be applied to indices in brackets.) The coefficient ${}^{j}C_5$ accounts for the simplification that only one transport equation for ${}^{v}\overline{E'}$ has been introduced instead of three for ${}^{j}\overline{E'}$:

$$ {}^{j}C_5 = \langle {}^{j}\overline{E'}\rangle/\langle {}^{v}\overline{E'}\rangle \tag{17} $$

The coefficients C_2 and C_{T2} are the dominating coefficients in equations 15. All other coefficients might have been absorbed in C_2 and C_{T2} to simplify the model, but this would restrict the applicability of the model to isotropic grids with $\Delta x_1 = \Delta x_2 = \Delta x_3$.

The inhomogeneous eddy diffusivities ${}^{ij}\mu^*$ and eddy conductivities ${}^{j}a_t^*$ are derived from modified common mixing length models:

$$ {}^{ij}\mu^* = \delta_{1i}\delta_{3j}\ell^2\left|\frac{\partial\,{}^{v}\overline{u_1}}{\partial x_3}\right| f(C_{10}, \Delta x_i) \tag{18a} $$

$$ {}^{j}a_t^* = \delta_{3j}\ell\ell_H\left|\frac{\partial\,{}^{v}\overline{\theta}}{\partial x_3}\right| f_H(C_{T10}, \Delta x_i) \tag{18b} $$

The characteristic length scales for the inhomogeneous model are the mixing lengths for momentum ℓ and for heat ℓ_H. Following Prandtl's arguments the characteristic velocity scale is $\ell|\partial\langle u_1\rangle/\partial x_3|$, and the temperature scale is $\ell_H|\partial\langle T\rangle/\partial x_3|$. The mixing lengths are well-known functions of the distance y from the wall and the dimensionless wall roughness h^+. In addition ℓ_H depends on the molecular Prandtl number of the fluid. We use a Nikuradse-Van Driest formulation for ℓ [29], and a Cebeci formulation for ℓ_H [36]. δ_{ij} is the Kronecker delta.

The damping functions f and f_H in Equations 18 depend on those mesh surfaces ${}^{j}F$ which contribute to the respective velocity and temperature fluctuations:

$$ f(C_{10}, \Delta x_i) = \mathrm{Min}\{1, C_{10}({}^{1}F^3F)^{1/4}F_0^{-1/2}\} \tag{19a} $$

$$ f_H(C_{T10}, \Delta x_i) = \mathrm{Min}\{1, (C_{10}C_{T10})^{1/2}({}^{3}F^2\,\Delta x_3)^{1/5}F_{H0}^{-1/2}\} \tag{19b} $$

The functions are designed so that for very coarse meshes the subgrid scale models become equal to the common models for time averaged turbulence (f, $f_H = 1$). This limiting state is determined by the normalization surfaces F_0 and F_{H0} which have to be deduced from empirical data. The coefficients C_{10} and C_{T10} are correction factors of order one which mainly account for uncertainties in the data for F_0 and F_{H0}.

The characteristic energy used in the isotropic parts of the subgrid scale model, Equation 15, is the subgrid scale kinetic energy ${}^{v}\overline{E'} = \frac{1}{2}\overline{({}^{v}u_i - {}^{v}\bar{u}_i)^2}$. Its isotropic part is calculated from the velocity fluctuations, ${}^{j}\overline{u_i'} = {}^{j}\overline{u_j} - \langle {}^{j}\overline{u_j}\rangle$, using an additional time-dependent three-dimensional transport equation which can formally be deduced from the basic equations (for simplicity we write ${}^{j}\overline{u_j}$ instead of ${}^{j}\overline{u_j'}$):

$$ \frac{\partial}{\partial t}{}^{v}\overline{E'} + \delta_j({}^{j}\overline{u_j}\,{}^{j}\overline{E'}) = P - {}^{v}\overline{\varepsilon} + \frac{1}{Re_0}\{(\delta_j\,{}^{j}\overline{u_i})(\delta_j\,{}^{j}\overline{u_i} + \delta_i\,{}^{i}\overline{u_j})\} + \delta_j\left\{\frac{1}{Re_0}\frac{\partial\,{}^{j}\overline{E'}}{\partial x_j} + \overline{{}^{j}u_i\frac{\partial\,{}^{j}u_j}{\partial x_i}} - {}^{j}\overline{u_i}\frac{\partial\,{}^{j}\overline{u_j}}{\partial x_i} - {}^{j}\overline{u_j'E'} - {}^{i}\overline{u_j'p'}\right\} \tag{20a} $$

where

$$P = -\overline{{}^{j}u_i' u_j'}\,{}^{j}\delta_j\,{}^{j}\overline{u_i} - \delta_{jk}\frac{Ra}{Re_0^2 Pr}\,{}^{j}\overline{u_j' T'} \tag{20b}$$

In the production terms the subgrid scale terms appear for which we have to introduce the complete set of model assumptions, Equations 13–19. Of course, all energy extracted by the subgrid scale model from the resolved scales has to act as the source term in the subgrid scale kinetic energy equation. Further unknowns are not only due to the well-known closure problem in the diffusion term, the averaged cross correlation between subgrid scale fluctuations of velocities, energy, and pressure, but in addition due to the subgrid scale part of the dissipation, ${}^{v}\overline{\varepsilon'}$, because the dissipation is mainly associated with high wave-number fluctuations. Thus, a dominating part of the subgrid scale model is the sink term in the subgrid scale energy equation.

The assumptions introduced for the closure terms follow the suggestions by Lilly [15]. The subgrid scale dissipation is formulated analogously to the Rotta model [37]. Additional corrections of the length scale in the dissipation model near the walls are necessary to balance the energy inflow by the inhomogeneous part of the subgrid scale model [21]. The terms introduced are analogous to those used by Jones and Launder [38]. The large-scale part of the dissipation is replaced by a simpler and less computer-time-consuming term recommended by the same authors. The final model equation is:

$$\frac{\partial}{\partial t}{}^{v}\overline{E'} + \delta_j\,{}^{j}C_5\,{}^{j}\overline{u}_j\,{}^{v}\overline{E'} = P - \frac{C_3\,{}^{v}\overline{E'}^{3/2}}{\min(h, C_{31}\ell)} - \frac{C_{32}\,{}^{v}\overline{E'}}{Re_0\min(h, C_{31}\ell)^2} - \frac{2}{Re_0}(\delta_3\,{}^{v}\overline{E'}^{1/2})^2 + \delta_j\left\{\left(\frac{{}^{j}C_5}{Re_0} + {}^{j}C_6({}^{j}F\,{}^{v}\overline{E'})^{1/2}\right)\delta_j\,{}^{v}\overline{E'}\right\} \tag{21}$$

The dissipation term containing the coefficient C_3 is dominant at large Reynolds numbers, and the one containing C_{32} at low Reynolds number turbulent flows. The coefficient C_{31} is only of relevance in the neighborhood of the walls where not the mean grid width

$$h = (\Delta x_1\,\Delta x_2\,\Delta x_3)^{1/3} \tag{22}$$

is a relevant length scale for the subgrid scale dissipation but the mixing length. Both scales bring the subgrid scale energy near zero, when very fine grids are used, and also in the viscous sublayer near the wall.

Calculation of Isotropic Model Coefficients

The procedure of calculating the coefficients of the isotropic model, Equations 15 and 21, includes all approximations needed to adapt the averaged equations to a finite difference scheme on a staggered grid as will be introduced later. Thus, most deficiencies implied by for example, linear averaging over neighbouring mesh cells, are taken into account in the final scheme.

The equation for C_2 can be found by introducing the finite difference representation of the isotropic model, Equations 13–15, into Equation 20 and taking the time mean value. In locally isotropic turbulence the mean values of the convection and diffusion terms vanish. The buoyancy terms mainly act on the large-scale structures and are therefore neglected in the calculation of the coefficients. An analogous procedure is applied to determine the equation for C_{12} from a transport equation for the subgrid scale temperature variances $\frac{1}{2}\overline{{}^{v}T'^2} = \frac{1}{2}\overline{({}^{v}T - {}^{v}\overline{T})^2}$ which is similar to Equation 20. This results in the following equations:

$$C_2 = \frac{\langle\varepsilon\rangle - \langle{}_2\bar{D}_{ij}^2\rangle/Re_0}{\gamma_1\,{}^{ij}C\,{}^{j}F^{1/2}\langle{}^{j}\overline{E'}^{1/2}\rangle\langle{}_2D_{ij}{}^2\rangle} \tag{23a}$$

$$C_{12} = \frac{\langle\varepsilon_{TH}\rangle - \langle{}_2\bar{D}_{Tj}^2\rangle/(Re_0\,Pr)}{\gamma_T\,{}^{j}C_T\,{}^{j}F^{1/2}\langle{}^{j}\overline{E'}\rangle^{1/2}\langle{}_2\bar{D}_{Tj}^2\rangle} \tag{23b}$$

The denominators are proportional to the production of subgrid scale kinetic energy and temperature variances. The time-averaged production terms have been split into products of two time averages to avoid triple correlations. The corresponding correction factors γ_1 and γ_T are therefore greater than or equal to one. These factors remain the only adjustable coefficients in the isotropic eddy diffusivity model. The numerators contain the respective subgrid scale dissipation written as the difference between total dissipation and dissipation resolved directly. The finite difference formulae for the strain tensor squared, ${}_2\bar{D}_{ij}{}^2$, and its counterpart in the heat flux model, ${}_2\bar{D}_{Tj}^2$, are:

$${}_2\overline{D_{ij}}^2 = \delta_j\,{}^{j}\overline{u}_i\overline{(\delta_j\,{}^{j}\overline{u_i} + \delta_i\,{}^{j}\overline{u_j})}^{j} \tag{24a}$$

$${}_2\overline{D_{Tj}}^2 = \delta_j\,{}^{j}\overline{T}\,\overline{\delta_j\,{}^{j}\overline{T}}^{j} \tag{24b}$$

The equations for C_3, C_{31}, and C_{32} can be deduced by termwise comparisons of Equations 20 and 21 for the limiting cases the model parts are valid for:

$$C_3 = h\frac{\langle{}^{v}\overline{\varepsilon'}\rangle}{\langle{}^{v}\overline{E'}^{3/2}\rangle} \approx \frac{h}{\gamma_2}\frac{\langle\varepsilon\rangle}{\langle{}^{v}\overline{E'}\rangle^{3/2}} \tag{25a}$$

$$C_{31} = \frac{\gamma_2 C_3\langle{}^{v}\overline{E'}\rangle^{3/2}}{\ell\langle{}^{v}\overline{\varepsilon'}\rangle} \tag{25b}$$

$$C_{32} = \frac{h^2\,Re_0\langle{}^{v}\overline{\varepsilon'}\rangle}{\langle{}^{v}\overline{E'}\rangle} \tag{25c}$$

Again, the correction factor γ_2 of order greater than or equal to one has been introduced to circumvent the problem of calculating triple correlations by the theory of isotropic turbulence. This factor is the only relevant adjustable parameter in the subgrid scale kinetic energy equation.

An equation for ${}^{j}C_6$ can in principal also be deduced by comparing the turbulent diffusion terms in Equations 20 and 21. However, these terms contain the unknown closure terms which cannot easily be calculated in isotropic turbulence. Therefore, a rather crude assumption has been introduced:

$${}^{j}C_6 \approx C_7\,{}^{j}C_5 \tag{26}$$

C_7 corresponds to a turbulent Prandtl number describing the ratio of the eddy diffusivities for subgrid scale energy and momentum transport. It was estimated to be $C_7 = 0.3$. The results have been found to be insensitive to this value.

Some approximate methods have been published to estimate the coefficients in subgrid scale models by the theory of isotropic turbulence, like the one by Lilly [15] for the momentum part of subgrid scale models, and the one by Schumann et al. [6] for the heat flux part of this model. These estimates are only valid for high Reynolds number flows and isotropic grids, and do not account for the assumptions introduced with the finite difference scheme. It has been found that the coefficients determined by this approximate method have to be fitted to the actual finite difference scheme used [39]. To circumvent this problem we will use the complete theory introduced by Schumann [13, 19] for the momentum fluxes. This method accounts for all approximations needed for a finite difference scheme on an anisotropic grid and includes molecular effects. The theory used here is documented in detail in Reference 21.

The key to the appplicability of the theoretical tools for isotropic turbulence is the circumstance, that in all model coefficients two-point correlations appear. One finds two-point correlations of volume- or surface-averaged variables of the form:

$$R_{ij}({}^{i}F, {}^{j}F, \underline{r}) = \langle{}^{i}\overline{u}_i(\underline{x})\,{}^{j}\overline{u}_j(\underline{x} + \underline{r})\rangle \tag{27a}$$

$$R_{TT}({}^{i}F, {}^{j}F, \underline{r}) = \langle {}^{i}\bar{T}(\underline{x})\,{}^{j}\bar{T}(\underline{x}+\underline{r})\rangle \tag{27b}$$

Two-point correlations can be evaluated if one assumes that the Kolmogorov and Batchelor spectra given in Equations 8 and 10 are valid for all wave-numbers. This assumption is justified because the energy-containing subgrid scale eddies follow these spectra in high Reynolds number large eddy simulations. (The influence of more realistic spectra on the coefficients has been considered in Reference 21.) For nonaveraged variables this results in:

$$\begin{aligned} R_{ij}(\underline{r}) &= \langle u_i(\underline{x})u_j(\underline{x}+\underline{r})\rangle \\ &= -\frac{18}{55}\alpha\Gamma(1/3)\langle\varepsilon\rangle^{2/3}\cdot\begin{cases} r^{2/3}(1-r_{ii}^2/(4r^2)) + R_{ij}(\underline{0}) & i=j \\ r_i r_j/(4r^{4/3}) & i\neq j \end{cases} \end{aligned} \tag{28a}$$

$$\begin{aligned} R_{TT}(\underline{r}) &= \langle T(\underline{x})T(\underline{x}+\underline{r})\rangle \\ &= -\tfrac{9}{20}\beta\Gamma(1/3)\langle\varepsilon_T\rangle\langle\varepsilon\rangle^{-1/3}r^{2/3} + R_{TT}(\underline{0}) \end{aligned} \tag{28b}$$

where $\Gamma(x)$ = gamma function

$$r = |\underline{r}| \tag{28c}$$

$$\varepsilon_T = 2a(\partial T/\partial x_j)^2 \tag{28d}$$

Two-point correlations of averaged variables, Equations 27, can be obtained by integrating over the mesh cell volumes or surfaces considered, e.g:

$$R_{ij}({}^{i}F, {}^{j}F, \underline{r}) = ({}^{i}F\,{}^{j}F)^{-1}\iint_{iF}\iint_{jF} R_{ij}(\underline{y}-\underline{x}-\underline{r})\,dF(\underline{y})\,dF(\underline{x}) \tag{29a}$$

$$R_{TT}({}^{i}F, {}^{j}F, \underline{r}) = ({}^{i}F\,{}^{j}F)^{-1}\iint_{iF}\iint_{jF} R_{TT}(\underline{y}-\underline{x}-\underline{r})\,dF(\underline{y})\,dF(\underline{x}) \tag{29b}$$

For most distance vectors $\underline{r}$ and orientations of the averaging surfaces ${}^{i}F$ these integrals can only be evaluated by numerical integrations. In some cases the integration range contains singularities. This would cause a tremendous numerical effort to evaluate the interlocked integrals if one would not use the weighting function formalism provided by Uberoi and Kovasznay [40, 13]. We give the final results which are deduced directly in a lengthy procedure without any further approximations. Equations 23 and 25a are replaced by:

$$C_2 = \frac{1-\alpha/\mathrm{Re}_0\,\Gamma(\frac{1}{3})\frac{18}{55}h^{-4/3}\langle\varepsilon\rangle^{-1/3}D2(\underline{\Delta x})}{(\alpha\Gamma(\frac{1}{3}))^{3/2}\frac{18}{55}(\frac{9}{20})^{1/2}f_1(\underline{\Delta x})\gamma_1} \tag{30a}$$

$$C_{T2} = \frac{\frac{1}{2}-\beta/(\mathrm{Re}_0\,\mathrm{Pr})\Gamma(\frac{1}{3})\frac{9}{20}h^{-4/3}\langle\varepsilon\rangle^{-1/3}DT2(\underline{\Delta x})}{\beta\alpha^{1/2}(\frac{9}{20}\Gamma(\frac{1}{3}))^{3/2}f_2(\underline{\Delta x})\gamma_T} \tag{30b}$$

$$C_3 = (\alpha\Gamma(\tfrac{1}{3})\tfrac{9}{20}E3(\underline{\Delta x}))^{-3/2}/\gamma_2 \tag{30c}$$

The functions D2, DT2, E3, f_1, $f_2 = f(\underline{\Delta x})$ contain the integrals just discussed depending only on geometrical details of the finite difference grid. The other important parameters are the constants α and β from the energy spectra. For high Reynolds number flows and coarse grids the terms in C_2 and C_{T2} containing the dissipation can be neglected. Then all coefficients depend only on grid parameters and the spectral constants. For low Reynolds number or low Peclet number flows, $\mathrm{Pe}_0 = \mathrm{Re}_0 \cdot \mathrm{Pr}$, or for very fine grids, these terms cannot be neglected and assumptions concerning the local dissipation of kinetic energy must be made. In this case C_2 and C_{T2} depend on local flow parameters. From the calculated values it can be seen whether one has to use the complete large eddy simulation scheme or whether one can perform a direct numerical simulation without the respective subgrid scale terms.

Similar expressions follow for ${}^{ij}C$, ${}^{j}C_T$, and ${}^{j}C_5$. These coefficients only depend on the local grid parameters. As an example, numerical results for all calculated coefficients are given in Table 1 for flows with $\mathrm{Re} = 5\cdot10^5$ and $5\cdot10^4$, and with $\mathrm{Pr} = 0.7$ using an isotropic grid and an anisotropic, cylindrical grid for an annulus. The constants in the spectra used are $\alpha = 1.5$ and $\beta = 1.3$. The calculated dominating coefficients C_2, C_{T2}, and C_3 increase with increasing mean grid width. The importance of the coefficients ${}^{ij}C$, ${}^{j}C_T$, and ${}^{j}C_5$ which purely depend on the finite difference scheme is evident from the results for the anisotropic grid.

The coefficients C_{31} and C_{32} from Equations 21 and 25 account for deviations from local isotropy at low Reynolds numbers and near the wall. These are determined by a simplified approach which allows for the incorporation of realistic measured spectra. Following the ideas of Lilly one can calculate the subgrid scale energy and dissipation from the energy spectra:

$$\langle {}^{v}\bar{E}'\rangle \approx \int_{\pi/h}^{\infty} E(k)\,dk \tag{31a}$$

$$\langle {}^{v}\bar{\varepsilon}'\rangle \approx 2\nu\int_{\pi/h}^{\infty} k^2E(k)\,dk \tag{31b}$$

Here, for E(k) we use the Pao spectrum [28] which is a good approximation to observed spectra in the high wave-number range:

$$E(k) = \alpha\langle\varepsilon\rangle^{2/3}k^{-5/3}\exp\{-\tfrac{3}{2}\alpha(k\eta)^{4/3}\} \tag{32}$$

The dissipation term in Equation 21 containing C_{32} should be dominating for very small Reynolds numbers (that means for $\mathrm{Re}_0 \approx 1/\eta \to 0$) and for very fine grids (that means for $h \to 0$). Therefore, C_{32} follows from a numerical integration of Equations 31 and 32 for these limits giving:

$$C_{32} = 20. \tag{33}$$

The coefficient C_{31} is active only in a narrow range near the wall. For this range nearly no experimental data on spectra exist. Therefore some empirical information has to be used to get an approximate value for the coefficient, e.g., a correlation from Lörcher [30] for the macroscopic length L needed in the Karman spectrum [28] has been used to approach a realistic spectral distribution in the low wave-number range. The value

$$C_{31} = \gamma_2 \cdot 0.74 \tag{34}$$

determined so far should be taken as a first guess. This had no influence on the simulations performed up to now [41], because the grids applicable on present-day computer systems are too coarse to resolve the wall region in high Reynolds number flows.

Having calculated all coefficients one has to calibrate the model by adapting the correction factors γ_1 and γ_T from Equations 30 and γ_2 from Equations 30c and 34. These factors have been determined in a sensitivity study. For this purpose high Reynolds number flows and coarse grids have been used [21, 41] because the subgrid scale models are important only under these conditions. It was the general result of the study that this one-equation model with problem- and grid-dependent coefficients is not very sensitive to the correction factors. This is in contrast to the higher sensitivity observed with other subgrid scale models [11, 32, 42]. The correction factor γ_1 from C_2 has been fixed at $\gamma_1 = 1.4$. The factor γ_2 from the dissipation model has nearly no influence on the results; therefore it remained unchanged at the expected value of $\gamma_2 = 1.0$. The coefficient γ_T from the heat flux model showed such a small influence at the Prandtl number of air, $\mathrm{Pr} = 0.71$, that a numerical fit was not possible [41]. This is due to the experimental evidence that at this Prandtl number relatively more energy is associated with the resolved scales in the temperature spectrum than in the kinetic energy spectrum [43]. At Prandtl numbers much smaller than one, this is even more pronounced and consequently a dependence on γ_T can almost not be detected [31]. Therefore γ_T was arbitrarily set equal to γ_1 such that the subgrid scale turbulent Prandtl number $\mathrm{Pr}_{SGS} = C_2/C_{T2}$ is in accordance with the spectral theory. Thus we have the following set of fixed

correction factors:

$$\gamma_1 = \gamma_T = 1.4 \tag{35a}$$

$$\gamma_2 = 1.0 \tag{35b}$$

These values have been used for pressure driven channel flows with a wide range of Reynolds and Prandtl numbers and of grid widths without observing any need to change them.

Determination of Inhomogeneous Model Coefficients

The coefficients of the inhomogeneous model (Equations 18, 19) cannot be calculated by a universal theory. They have to be determined by an empirical approach. Here, we follow the arguments given in Reference 21.

The normalization surfaces F_0 and F_{110} in the damping functions of the inhomogeneous model (Equations 19), should be set equal to those values of ${}^3F$ for which the subgrid scale shear stress $\overline{{}^3u_1 u_3}$ and the heat flux $\overline{{}^3u_3 T}$ become equal to the total turbulent shear stress and heat flux calculated by time averaging. With this definition the correction factors C_{10} and C_{110} would be of order one.

Thus F_0 can be found by looking for the smallest surface ${}^3F$ over which the two-point correlation $R_{13}(x_1, x_2)$ is zero. Unfortunately there are not enough data for R_{13} in channel flows to determine this value. Therefore the better known data for $R_{11}(x_1)$ and $R_{11}(x_2)$ have been used to roughly estimate F_0. From the experiments by Comte-Bellot [44] one gets:

$$F_0 = \Delta x_1 \, \Delta x_2 = 1.6 \cdot 0.8 = 1.28 \tag{36}$$

This value shows that the subgrid scale model reaches the limiting case of being equivalent to a Reynolds-type model when the complete channel is recorded by just one mesh cell. In all realistic applications the importance of the inhomogeneous model is drastically reduced; following the definition of the damping function, Equation 19, the relative importance of the model is roughly proportional to the dimensionless mean grid width h.

The surface F_{110} should be equal to the smallest surface ${}^3F$ over which the two-point correlation $R_{33}(x_1, x_2)$ is zero. Again one does not find enough data for R_{33} in channel flows for different Prandtl numbers to determine this value. Especially the increase in F_{110} with decreasing Prandtl numbers, which is obvious from combined large eddy/direct numerical simulations [21], could not be quantified. Thus one has to use the crude assumption

$$F_{110} = F_0 = 1.28, \tag{37}$$

which implies that the damping function is not explicitly dependent on the Prandtl number.

The values of the corresponding correction factors have been determined by a sensitivity study [21]. It has been found that the inhomogeneous model is an important part of the model. It makes the coefficients of the isotropic model universal. On the other hand a low sensitivity on the coefficients C_{10} and nearly no sensitivity on C_{110} have been detected in the range of realistic, expected values of the coefficients. The values finally used are:

$$C_{10} = 2.0 \tag{38a}$$

$$C_{110} = 1.0 \tag{38b}$$

The value for C_{110} has been set arbitrarily to the expected value because the scatter of experimental data on temperature field statistics does not allow for a finer adjustment.

The missing dependence of F_{110} on the molecular Prandtl number has to be accounted for by reducing C_{110} with decreasing Prandtl numbers. In all calculations performed with the model the following rule gave sufficient results [31]: The value $C_{110} = 1.0$ is used if the calculated coefficient

Table 1
Subgrid Scale Coefficients*

	h	C_2 ($\gamma_1 = 1.4$)	C_{T2} ($\gamma_T = 1.4$)	C_3 ($\gamma_2 = 1$)	$_{ij}C$	$_{ij}C$ ($i \neq j$)	$_{ij}C_T$	$_{ij}C_S$	j, ij
isotropic grid	0.0625	0.0506	0.1281	0.6336	1.474 1.474 1.474	0.823 0.823 0.823	1.0 1.0 1.0	0.828 0.828 0.828	1, 12 2, 13 3, 23
annulus, $k = 1$	0.0607	0.0449	0.1179	0.5625	1.760 1.450 1.534	0.782 0.996 0.692	1.332 0.793 1.012	0.672 0.937 0.851	1, 12 2, 13 3, 23
annulus, $k = KM$	0.0928	0.0476	0.1229	0.5974	1.520 1.626 1.430	0.955 0.731 0.788	1.038 1.196 0.833	0.824 0.735 0.915	1, 12 2, 13 3, 23

* *Calculated at* $Pr = 0.7$ *on an isotropic grid with* $\Delta x_i = 1/16$, $Re = 5 \cdot 10^5$, *and on a grid in an annulus with* $R_1/R_2 = 0.25$, $\Delta x_1 = 0.1$, $\Delta\phi = \pi/32$, $\Delta x_3 = 1/16$, $Re = 5 \cdot 10^4$, $k = 1$ *denotes the mesh cell near the inner wall,* $k = KM$ *the one near the outer wall.*

C_{T2} of the isotropic model is greater than zero everywhere in the channel. If C_{T2} is equal to zero anywhere in the channel then the inhomogeneous heat flux model is neglected, that means $C_{T10} = 0$. Another more continuous adaption might be to reduce C_{T10} by multiplying it with a reduction factor deduced from the isotropic heat flux model in the near wall range:

$$C_{T10}(Pr \ll 1) \approx 1.0 \cdot C_{T2}(Pr \ll 1)/C_{T2}(Pr = 1) \tag{39}$$

An analogous approach can also be used in the inhomogeneous shear stress model to get an automatic transition to direct numerical simulations.

The inhomogeneous model and the terms in the dissipation model accounting for near wall effects are only valid for pressure-driven channel flows and comparable flow problems. In all other cases, in which the Prandtl mixing length approach is not meaningful, the coefficients C_{10}, and C_{T10} have to be set to zero and C_{31} to infinity.

Finite Difference Scheme

There are many methods to integrate the averaged basic equations in space and time. An overview on some methods is given in Reference 7. It is still an art to construct such schemes and to adequately apply them. Here we restrict ourselves to present the procedure we have used [6].

Spatial Discretization

Starting from the volume-averaged Equations 6, which are still in an exact form, one is inclined to use a staggered grid system (Figure 2). There, one does not need any approximation to calculate the continuity equation. That means the continuity Equation 6a is exact even in its numerical representation. This is the reason why staggered grids are used so often in computational fluid dynamics.

Approximations are needed, however, for the large-scale part of the convective terms (Equations 7) appearing in the averaged momentum and thermal energy equations. These terms must be known at positions not coinciding with the positions of the corresponding variables in the staggered grid. They can be evaluated by the usual algebraic averages $\bar{y}^i$ of the values at two neighboring positions in the i-th direction. In the x_3-direction we allow for nonequidistant grids. In this direction a weighted linear average $\bar{y}^j$ is used to account for variable mesh widths Δx_j:

$$\bar{y}^j(x_j + \tfrac{1}{2}\Delta x_j) \simeq \frac{y(x_j + \Delta x_j)\,\Delta x_j(x_j + \Delta x_j) + y(x_j)\,\Delta x_j(x_j)}{\Delta x_j(x_j + \Delta x_j) + \Delta x_j(x_j)} \tag{40}$$

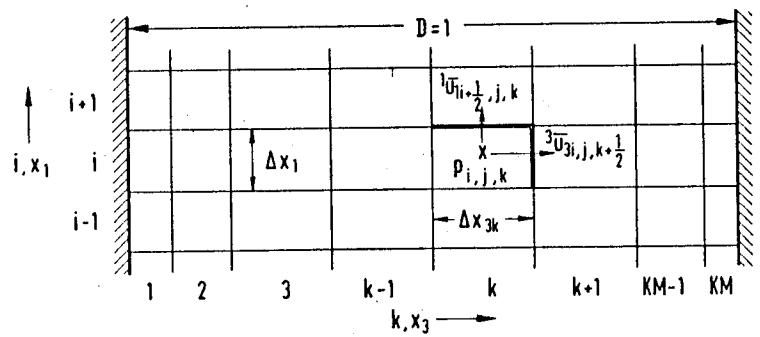

Figure 2. Staggered grid. ${}^i\bar{u}_i$ is fixed at the surfaces of the mesh cells, ${}^v\bar{p}$, ${}^v\bar{E}'$, ${}^v\bar{T}$ at the center.

This results in the following approximations for the resolved parts of the convective terms:

$${}^i\overline{u_i}\,{}^j\overline{u_j} \approx \overline{{}^i\overline{u_i}}^j\,\overline{{}^i\overline{u_j}}^j \tag{41a}$$

$${}^i\overline{u_j}\,{}^j\overline{T} \approx {}^i\overline{u_j}\,\overline{{}^v\overline{T}}^j \tag{41b}$$

Similar approximations have to be used for the subgrid scale models and for the production term of the subgrid scale energy equation as has already been accounted for in the equations defining the model coefficients.

The spatial derivatives still remaining in the diffusive terms in Equation 6 are replaced by the finite difference operator given in Equation 5.

The complete spatial finite difference scheme used is a second-order energy-conserving scheme. It could be shown in Reference 6 that in practice schemes remain second-order schemes on suitable non-equidistant grids in which neighboring grid widths differ by not more than a factor of two if the grid width is changing continuously. Such grids can be generated by relationships as tested by Agrawal and Peckover [45] for wall bounded flows.

The resultant finite difference equations are the same as those used by Deardorff [16] for Cartesian and by Williams [46] for cylindrical coordinates, as far as the gross scale velocities are concerned. Therefore, volume balance and filter averaging procedures give the same result in this respect.

Boundary Conditions

The physical boundary conditions for channel flows are the no-slip condition at the walls and space- and time-dependent conditions for all flow variables at the inlet and the outlet of the channel.

Difficulties with finite difference schemes are usually raised by the common no-slip condition:

$$\underline{u}|_w = 0 \tag{42}$$

This condition can be realized on a staggered grid without any further approximations. The ${}^1\bar{u}_1$ and ${}^2\bar{u}_2$ values are defined on grid cell surfaces which do not coincide with the wall and therefore need not to be specified. The ${}^3\bar{u}_3$ component is defined exactly in the plane of the walls (see Figure 2) and is therefore equal to zero.

The only terms of the basic equations in which approximations have to be introduced are the normal flux components in the diffusive terms:

$${}^3\bar{\tau}_{i,3} = -\nu\,{}^3\overline{\partial u_i/\partial x_3}, \qquad i = 1, 2 \tag{43a}$$

$${}^3\bar{q} = -a\,{}^3\overline{\partial T/\partial x_3} \tag{43b}$$

For laminar flows, and for all turbulent flows in which the viscous sublayer can be resolved by the finite difference grid, an obvious approximation is

$${}^3\bar{\tau}_{i,3w} \approx -\nu\frac{{}^i\bar{u}_i|_1}{\left(\frac{\Delta x_3}{2}\right)}, \qquad i = 1, 2 \tag{44}$$

where ${}^i\bar{u}_i|_1$ is the velocity in the middle of the first wall adjacent grid cell (k = 1 in Figure 2). Similarly the general boundary condition

$$a_w T - b_w a\,\partial T/\partial x_3 = c_w \tag{45}$$

is used to approximate the normal heat flux at the wall:

$${}^3\bar{q}|_w = -a\frac{2(a_w\,{}^v\bar{T}|_1 - c_w)}{\Delta x_3 a_w + 2b_w a} \tag{46}$$

These approximations suffice for laminar and low Peclet number turbulent flow in which the temperature profile is linear near the walls.

The truncation errors of the approximation Equations 44 and 46 are only of first order in Δx_3 [47]. This reduces the effective convergence order of the total finite difference scheme slightly from second order as it is prescribed by the scheme for inner mesh cells. The actual effective convergence order can only be determined by extensive numerical tests for the problem actually considered, because the truncation errors depend on the local flow variables. This in practice hinders one from extrapolating results of direct numerical simulations for nonlinear flow problems to accurate results for zero grid width as has been the experience of Churchill et al. [48].

For turbulent flow simulations on coarse grids in which the viscous or conductive sublayer is not resolved one has to use other approximations for Equations 43. In such cases the region of turbulence production has to be modeled using additional empirical information on the velocity and temperature distribution within the near wall mesh cell. The following assumptions guarantee that the wall shear stresses and heat fluxes are in accordance with the inhomogeneous subgrid scale model and with common turbulence models at least with respect to the predicted statistical mean values:

$$ {}^3\overline{\tau_{1,3}}|_w = \frac{\langle \tau_{w1} \rangle}{\langle {}^1u_1|_1 \rangle} {}^1\overline{u_1}|_1 \qquad \text{(not for } u_2, u_3\text{)} \tag{47} $$

Here, $\langle {}^1\overline{u_1}|_1 \rangle$ is a mean value of the calculated axial velocity in the wall adjacent grid cell; the average is taken over the plane parallel to the wall and in case of stationary turbulence over the past simulation results. The mean wall shear stress $\langle \tau_{w1} \rangle$ is approximated by the logarithmic law of the wall for smooth and rough walls using the calculated $\langle {}^1u_1|_1 \rangle$ as input value. The local wall shear stress fluctuates around this calculated mean value in phase with the wall adjacent local main velocity. This is in rough agreement with the data by Eckelmann [49], but it does not account for the small phase shift between u_1 and $\tau_{1,3}|_w$ observed there. Similarly, the local wall heat flux at large Peclet number flows is specified as:

$$ {}^3\overline{q}|_w = \langle q_w \rangle \frac{{}^v\overline{T}_1 - T|_w}{\langle {}^v\overline{T}_1 - T|_w \rangle} \tag{48} $$

Here, either $\langle q_w \rangle$ or $\langle T_w \rangle$ is prescribed from the underlying physical boundary condition. The unknown average is determined from the logarithmic temperature law of the wall integrated over the wall adjacent grid cell. The procedure accounts for influences of wall roughness and molecular Prandtl number. It is described in detail in Reference 21, together with the analogously formulated boundary conditions for the subgrid scale energy Equation 21.

The specification of inlet and outlet conditions is a general problem in computational fluid dynamics. It is an even harder problem in case of direct or large eddy simulation, because here one has to specify realistic turbulence fields for all variables at the inlet and the outlet for every mesh cell and for every time step. There is no general solution available to this problem. A widely used assumption is that all velocity components, pressure, and temperature are periodic in the main stream direction. In the TURBIT code [35] which we use here periodicity is also assumed in the spanwise direction. The respective periodicity lengths

$$ X_1 = IM\,\Delta x_1 \tag{49a} $$

$$ X_2 = JM\,\Delta x_2 \tag{49b} $$

are prescribed in terms of the number of mesh cells IM and JM, and the mesh widths Δx_1 and Δx_2. They have to be chosen large enough to allow for zero two-point correlations of all flow variables within the considered volume. That means the largest dominating scales have to be recorded especially those in the spatiously correlated pressure field. This requirement is of quite different importance for different types of flows. Whereas forced channel flows show weak influences on too-short periodicity lengths [21], natural flow problems have been found to be very sensitive on insufficiently chosen periodicity lengths [50].

The periodicity assumptions do not allow for mean gradients in the respective spatial directions. This problem can be circumvented by transformations of the dependent variables with the mean gradient, or in a more approximate, but easier manner by a Galilei transformation to a grid moving with the mean velocity [21]. The latter approach replaces the investigation of a variation in space by an approximately similar variation in time.

Time Integration

In direct and large eddy simulations in contrast to the Reynolds models one cannot be interested in using very large time steps because this would induce a time filtering in addition to the volume filtering. As a consequence the importance of the subgrid scale terms would be increased towards the importance of the closure terms in Reynolds models. This would also increase the effort to determine the model coefficients and would reduce the degree of universality reached by purely volume averaging. Thus by filtering reasons one is bounded to time steps Δt for which transport lengths $u \cdot \Delta t$ are smaller than the grid width Δx. This so-called Courant condition is also needed to get explicit schemes stable. It is this coincidence of requirements which allows application of simple explicit finite-difference schemes to most flow simulations.

In an explicit scheme, as it will be used here, the diffusive terms must be treated by first-order schemes for stability reasons. The time-differencing scheme for the dominant convective terms should be at least of second order because first-order schemes, which have to use upwind differences for stability, induce strong numerical damping [51]. Following Deardorff [16] a mixed procedure is employed in which an explicit first-order Euler scheme is used for the diffusive terms, whereas the second-order leapfrog scheme is used for the convective terms. This results in the following finite-difference scheme, written without space-averaging bars, where the superscript n refers to the time step $t^n = n\,\Delta t$:

$$ (\tilde{u}_i^{n+1} - u_i^{n-1})/2\Delta t = -\delta_j(\overline{u}_i^j \overline{u}_i^j)^n + \delta_j\left(\frac{1}{Re_0}\delta_j u_i - {}^j\overline{u_i' u_j'}\right)^{n-1} + P_r \delta_{i1} - \frac{Ra}{Pr\,Re_0^2}(T_{ref} - T)^n \delta_{i3}, \qquad i = 1, 2, 3 \tag{50a} $$

$$ (T^{n+1} - T^{n-1})/2\Delta t = -\delta_j(u_j \overline{T}^j)^n + \delta_j\left(\frac{1}{Pr\,Re_0}\delta_j T - {}^j\overline{u_j' T'}\right)^{n-1} + \dot{Q} \tag{50b} $$

The leapfrog scheme is bound to produce spurious $2\Delta t$-oscillations [15] which can be kept sufficiently small by means of an averaging step every $N_L \approx 20$–60 time steps. The procedure starts each leapfrog loop with an Euler scheme for all terms. The different integration methods are combined in the computer code to one unique scheme [16].

In Equation 50a the fluctuating part of the pressure gradient has been neglected. Therefore, $\tilde{u}_i^{n+1}$ is only a tentative result; it does not satisfy the continuity equation.

The time step permissible for this special finite difference scheme has been determined by Schumann [52] by means of a linear stability analysis giving:

$$ \Delta t \le \frac{1}{2}\left(\frac{|u_i|}{\Delta x_i} + 4\frac{\max(\nu + {}^1\mu^*, a + {}^3a_i^*)}{\Delta x_i^2}\right)^{-1} \tag{51} $$

The actually used time steps are about 50% to 80% of the value calculated from Equation 51.

Pressure Calculation

The method to compute the turbulent pressure and the final velocity field follows the proposals by Chorin [53] and Amsden and Harlow [54]. The tentative velocity field $\tilde{u}$ does not satisfy the continuity equation. It differs from the correct velocity field by the pressure gradient:

$$ u_i^{n+1} = \tilde{u}_i^{n+1} - 2\Delta t \frac{1}{\rho}\delta_i p^{n+1} \tag{52} $$

The factor 2 corresponds to a leapfrog step. $\tilde{n}$ denotes that the pressure is not strictly assigned to the actual time level but rather to some intermediate level. Now the continuity equation in its discretized form Equation 6a is applied to the new velocity field, Equation 52. This gives the following Poisson equation for the pressure:

$$\frac{1}{\rho}\delta_i\delta_{ii}p^{\tilde{n}+1} = \delta_i\tilde{u}_i^{n+1}/(2\Delta t) \tag{53}$$

At the walls one specifies the no-slip condition not only for the correct u_3 field, but also for the tentative one, $\tilde{u}_3|_w = 0$. Therefore one gets a Neumann-type boundary condition for the pressure from Equation 52:

$$\delta_3 p|_w = 0 \tag{54}$$

This approximate boundary condition is valid as long as the viscous terms are treated explicitly. Otherwise a more complicated formalism as published by Kleiser and Schumann [55] is necessary.

The set of algebraic equations for the pressure values in each grid cell resulting from Equation 53 is solved very efficiently by means of Fast Fourier Transforms in the periodic x_1 and x_2 directions and by Gaussian elimination for the remaining sets of tridiagonal systems [19]. For other more complicated geometries similar fast elliptic solvers are available, e.g. from Buzbee et al. [56] and from Schumann and Benner [57].

This pressure calculation scheme ensures that the velocity field satisfies the continuity equation exactly, except for round-off errors, and independently of the departure from continuity in the previous or initial time level velocities; so the accumulation of divergence errors is avoided.

Initial Conditions

To start the time integration of the basic equations initial values are required for the velocity, temperature, and subgrid scale energy fields. These may be chosen arbitrarily because statistical mean values of the simulated turbulence fields do not depend on the initial conditions after some time of development. Two important exceptions exist. In cases of investigating laminar to turbulent transition flows one must not use purely laminar or regular two-dimensional initial conditions. Such a flow would remain laminar as the simulations use clean boundary conditions. The flow will only become unstable if sufficient energy is introduced by prescribing a disturbance which makes the flow three-dimensional [33]. In cases in which several stable flow regimes exist one should not start from regular vortex systems which are meaningful in this parameter range and have too little energy in three-dimensional disturbances. In such cases one cannot be sure to reach the most probable state of flow [50, 58].

The most important demand for initial conditions is due to practical reasons. In order to shorten the computer time required to reach fully developed equilibrium, the statistical properties of the initial flow fields should be very close to the steady-state solutions. Unfortunately initial conditions for all higher-order simulations cannot be derived from experimental results. These never contain enough information to construct complete initial fields. Thus, one has to specify initial fields as realistic as possible.

One procedure of specifying initial fields starts from generating random fluctuations. The fluctuation amplitudes are roughly adapted according to the root mean square values of the expected spatial distributions. Finally the mean values of main velocity and temperature over planes parallel to the walls are prescribed by empirical relations, e.g. by means of the logarithmic laws of the wall. For some integration schemes, but not for the one described here, one has additionally to ensure that the continuity equation is satisfied. This is a simple procedure which does not give too bad initial conditions and which is therefore widely used.

In some more extended procedures the random fluctuation fields are firstly modified to have realistic energy spectra [19, 59] and then were adapted to the problem following the method just mentioned. There are even attempts to prescribe cross correlations, especially the radial shear stress [25]. This should be the most advantageous method of specifying initial conditions because the second-order moments of the turbulence fields need much more time to reach an equilibrium state than the first-order moments. Nevertheless these initial fields do not allow for considerably shorter computation times. It is impossible to prescribe initial fields which have realistic distributions for all relevant moments, say the first, second, and third-order moments. Therefore all simulations start with reordering the carefully specified initial fields and thus destroy them.

The only procedure to deduce initial conditions which can somewhat reduce the computing time is to use former simulation results for similar problems on similar grids. These results should be altered as little as possible to adapt them to the problem to be investigated. Such initial fields are very close to realistic turbulence fields and need short computing time for redistribution and redevelopment of an equilibrium state [19, 21, 31, 35, 42].

An initial spatial distribution for the subgrid scale kinetic energy can easily be deduced from a simplified steady version of Equation 21. The balance of production and dissipation allows for calculating an approximate initial energy field from the initial velocity field specified before.

Evaluation Procedure

Starting from the initial conditions just defined, the set of finite difference equations has to be integrated in time until largely equilibrium conditions or steady-state conditions in a statistical sense have been established for a period suitable for evaluation of the still time-dependent turbulence fields. For quantitative evaluation of the numerical results and for comparisons with statistical data determined experimentally, the non-steady-state numerical results must be averaged appropriately. The average values can be formed over the planes parallel to the walls as have also been used in the boundary conditions (Equation 47). In addition, these values can be averaged over those for other time steps within the final time interval. We usually average over about 10 to 40 time steps equidistantly distributed by an interval given by the number of leapfrog time steps N_L. On not too coarse grids this gives standard deviations for the evaluated mean velocities and temperatures of typically 0.5 to 6‰, and about 1% to 12% for higher-order moments [31]. The accuracy can be increased by considering larger time intervals or by increasing the periodicity lengths.

When analytical expressions shall be evaluated which are formulated in terms of the calculated flow variables, one has to deduce finite difference representations for these terms. One should use identically the same procedure given earlier as has been applied to get the numerical simulation scheme. Only this ensures that the physical meaning of the variables used in the simulation is consistent with the one needed in the evaluation formalism.

All data determined from the simulated turbulence fields are goverped only by those scales which have been resolved by the grid. This does not bring any problems with direct numerical simulations because no relevant information has been lost in the subgrid scales. The resolution of the grids is at least comparable to that of measuring sensors. Therefore, the filtered data calculated by the finite difference scheme can be taken to be equivalent to the nonfiltered physical data. In case of evaluating large eddy simulation results one directly gets only data determined by the large scales. For some data one can approximately add the respective small scale part; e.g., the large-scale kinetic energy can be complemented by the local mean value of the subgrid scale kinetic energy; or the evaluated root mean square values of the velocity fluctuations can be completed by adding the root of two thirds of the mean subgrid scale energy which follows from assuming isotropic subgrid scales; or with a similar approach given in Reference 21, the evaluated temperature variances can be completed; or the inhomogeneous parts of the subgrid scale model can be added to the evaluated radial shear stress and heat flux. In most other cases such complements accounting for the subgrid scales cannot be formulated. Therefore, to keep the corresponding errors small, the large eddy simulation method should only be used to investigate phenomena and data which are mainly dependent on the resolved scales.

The investigation of flow phenomena can only be performed if suitable plot software and hardware is available to visualize instantaneous two-dimensional or three-dimensional representations of the calculated flow fields. The presentation of the data in the form of movies is highly desirable to investigate time-dependent flow structures. These tools are also necessary in testing the numerical model, because many errors in the scheme or deficiencies in the subgrid scale models lead to unphysical regular structures in the computed flow fields.

Thus the expenditure to prepare computer codes for evaluations of the data computed by direct or large eddy simulations can be approximately comparable to that which is needed for the development of the simulation scheme.

APPLICATIONS

The direct numerical simulations of channel flows realized up to now have mainly been in the field of fundamental research of the laminar to turbulent transition in channels. There, especially the buoyancy driven flows in horizontal plane channels, have such low grid requirements as just can be met on today's computer systems. The first direct numerical simulations using finite difference schemes have been performed for Rayleigh-Bénard convection in infinite fluid layers, e.g. by Lipps and Somerville [60], Ozoe et al. [61], and Lipps [62]. The work by Hathaway and Somerville [63] includes tilted rotation vectors. Oertel and his coworkers also consider transition flow, but in horizontal rectangular enclosures [64], in tilted enclosures [65], and in rotating boxes [66]. The simulations by the present author have been extended to the fully turbulent regime of Rayleigh-Bénard convection [50, 58] and of internally heated horizontal fluid layers [67, 68].

The first large eddy simulations have been performed by Deardorff [16] for pressure-driven channel flows at infinite Reynolds number by means of finite-difference schemes. The method includes models for the viscous sublayer and uses constant subgrid scale coefficients. It has been applied to investigations of Lagrangian turbulent quantities by Peskin [69]. The method has been extended to account for large but finite Reynolds numbers and for the influence of the finite-difference scheme on the subgrid scale coefficients by Schumann [19], and to account for low Reynolds number flows by the author [21]. This scheme has been used to investigate wall pressure fluctuations [41, 70] and the related rod vibration problem in an annulus [20], to investigate flows in partly roughened channels with secondary currents [22], and to investigate a plane thermal mixing layer in a buoyant shear flow [35]. Similar schemes with wall assumptions and with constant coefficients have been used in micrometeorology. For example, the work by Deardorff [17, 71, 72], by Schemm and Lipps [18], and by Sommeria [33] gained the experience with subgrid scale models of different closure order. Baron and Laurence [73] report on large eddy simulations of a wall-bounded turbulent jet flow using the Smagorinsky model.

The first large eddy simulation that computed rather than modeled the flow in the immediate neighborhood of the wall was that by Moin et al. [25], followed by the calculations by Moin and Kim [42] carried out on the ILLIAC IV computer with up to 128·64·63 grid points. These simulations and the one by Kim [74] for a rotating channel have been used to study turbulence structures and to calculate statistical data needed for the calibration of Reynolds models. Their subgrid scale model is very similar to the one discussed earlier, but the coefficients do not depend on the local grid and flow parameters. All these dependencies have been accounted for in the simulations of turbulent temperature fields of liquid metal flows by the author [21, 31]. In these simulations a combination of a large eddy simulation of the velocity field and a direct simulation of the temperature field automatically followed from the theory to calculate the subgrid scale model coefficients.

Subsequently three examples will be reported in which the methods discussed earlier and realized in the TURBIT computer code [35] are applied. In the first example an internally heated horizontal fluid layer is investigated by means of direct numerical simulations. The second example, the investigation of annular liquid metal flows, is in the transition range from direct to large eddy simulations of turbulent temperature fields. In the third example a prototypical engineering problem, a plane mixing layer in a strongly buoyancy-influenced vertical shear flow, is efficiently solved by means of the large eddy simulation technique on a coarse grid.

Turbulence Data in Internally Heated Horizontal Fluid Layers

The Problem

The convection in horizontal fluid layers with internal heat generation is of interest as a model for certain environmental, geophysical, astrophysical, and nuclear engineering heat transfer problems. For the numerical description of the turbulent heat transfer in such layers two-dimensional

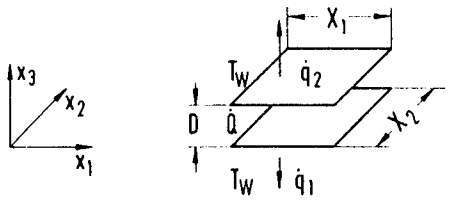

Figure 3. Specifications for the internally heated fluid layer.

simulations [75, 76] and statistical turbulence models based on the eddy conductivity concept [77, 78] and on the k-ε model [79] have been used. From experiments as in Reference 80 heat transfer data across the boundaries and a few temperature profiles have been obtained, from which some turbulent heat flux profiles have been estimated in Reference 81. This information is not sufficient to determine the coefficients used in higher-order turbulence models. The only available data on turbulence statistics for this type of flow have been deduced by direct numerical simulations of fully turbulent convection at moderate Rayleigh numbers by means of the TURBIT-code [67, 68]. Here some additional data will be given.

Case Specifications

A plane horizontal channel is considered with periodic boundary conditions in both horizontal directions (see Figure 3). The fluid with Pr = 6 is internally heated by the volumetric heat source $\dot{Q}$. The heat is removed from the channel by prescribing equal wall temperatures at both walls.

The spatial discretization required for direct numerical simulations is deduced by application of the criteria given in References 50 and 67: The maximum allowable mean grid width h_{max} follows from the subgrid scale coefficient C_{r2} (Equation 30b), which must be zero. For an isotropic grid the numerator reduces to:

$$h \le h_{max} = 3.45(a^3/\varepsilon)^{1/4} \tag{55}$$

The dissipation has been calculated to be largest near the upper wall. Its maximum value can be approximated by

$$\varepsilon_{max} \approx (Nu_2 - Nu_1)Ra/(Re_0^3\, Pr^2\, Da_0) \tag{56}$$

The Nusselt numbers are estimated from the empirical correlations given by Jahn [82]. This results in the largest reasonable mean grid width shown in Figure 4. The allowable vertical grid width near the lower wall, h_{3w1}, and near the upper wall, h_{3w2}, is shown in the same figure. It is deduced by discretizing the thermal boundary layers by three nodes:

$$h_{3wi} = D/(3Nu_i) \qquad i = 1, 2 \tag{57}$$

The periodicity lengths X_i required can be chosen to be constant and equal to two times the critical wavelength λ_c because experiments (e.g., by Kulacki and Goldstein [80] and by Jahn [82]) show that the largest scales of this type of flow decrease with increasing Rayleigh number. With $\lambda_c = \pi/2$ as calculated by Tveitereid [83] this gives $X_i = \pi$. Therefore the node numbers N_i required in the horizontal directions are:

$$N_i = X_i/h_{max} \tag{58}$$

The node number N_3 required in the vertical direction can be estimated for a nonequidistant grid by starting with h_{3wi} from the walls and doubling the grid width up to the possible value h_{max}. As shown in Figure 4, at the critical Rayleigh number, $Ra_{cr} = 37{,}400$, one needs only nine mesh cells in each horizontal direction, and six in the vertical one for direct simulations of this flow. At $Ra = 10^6$ one needs $32 \cdot 32 \cdot 12$ mesh cells, which is still within the possibilities of available computers. The upper bound for tolerable direct simulations to be performed on the newest computer

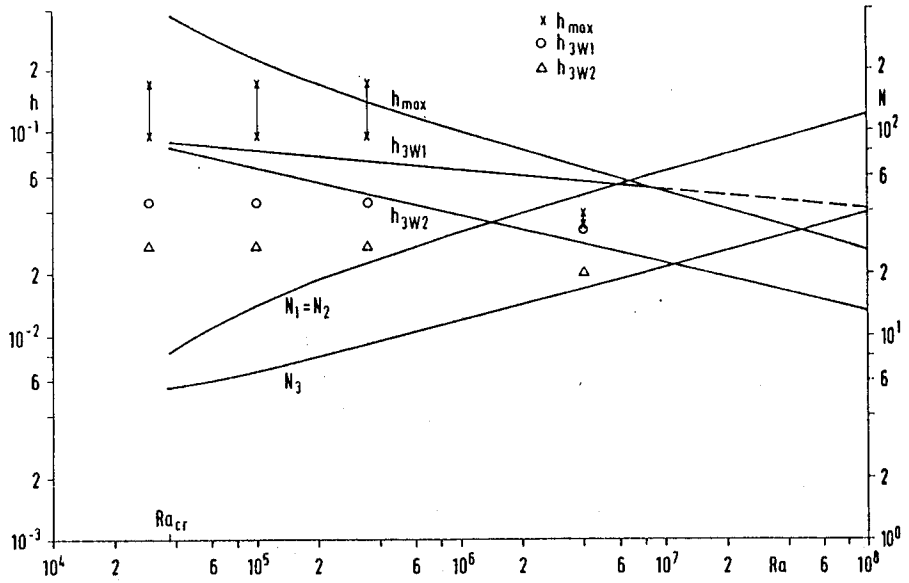

Figure 4. Grid parameters required and used for direct numerical simulations of the internally heated fluid layer.

systems may be reached at Ra $\approx 10^8$, because these simulations would require $120 \cdot 120 \cdot 40$ mesh cells.

The grids actually chosen for our simulations are specified in Table 2. They are compared in Figure 4 to the requirements just given. All grid widths are sufficient to neglect the subgrid scale models and to use the linear wall approximations (Equations 44–46). Thus the simulations do not depend on any empirical parameter.

The initial conditions are zero velocities all over the channel and roughly approximated vertical mean temperature profiles on which random fluctuations are superposed with a maximum amplitude of 25% of the time mean temperature difference $\Delta T_0 = \langle T_{max} - T_w \rangle$. The normalization of all variables is given earlier.

Verification

The simulations have been performed for the number of time steps N_t within the dimensionless time intervals t_{max} as given in Table 3. The computing times are also included in this table as the number of time steps N_{tav} distributed within the final time interval t_{av}, over which mean values

Table 2
Case Specifications for the Internally Heated Fluid Layers

Ra	Da_0	N_1	N_2	N_3	Δx_1	Δx_2	Δx_{3w1}	Δx_{3w2}	Δx_{3max}
$3 \cdot 10^4$	8.0	16	8	16	0.175	0.175	0.044	0.027	0.158
$1 \cdot 10^5$	8.35	16	16	16	0.175	0.175	0.044	0.027	0.158
$3.5 \cdot 10^5$	10.26	16	16	16	0.175	0.175	0.044	0.027	0.158
$4 \cdot 10^6$	15.72	64	64	32	0.0438	0.0438	0.0325	0.020	0.0325

Table 3
The Time Intervals Used for the Direct Simulations of the Internally Heated Fluid Layer, the Corresponding CPU Times, and the Final Time Intervals Used for Evaluation

Ra	N_t	t_{max}	CPU-time [h]	N_{tav}	Δt_{av}
$3 \cdot 10^4$	2400	12.0	0.61/IBM 168	21	3.57
$1 \cdot 10^5$	5760	44.8	2.96/IBM 168	26	8.15
$3.5 \cdot 10^5$	5760	75.6	2.96/IBM 168	26	13.75
$4 \cdot 10^6$	4040	40.2	38.2 /IBM 3033	14	5.62

have been taken in the evaluation procedure. The problem times are sufficiently long to get a fully developed flow within the time intervals used for evaluation.

For a qualitative verification of the results we consider the calculated structure of the flow. At the smallest Rayleigh number, $Ra = 0.8Ra_{cr}$, the initially developed velocity field goes to zero. The temperature distribution is governed by conduction and not distorted by convection. The fluid layer is stable against the perturbation introduced by the initial conditions as expected for a subcritical Rayleigh number. For $Ra = 2.7Ra_{cr}$ a steady-state arrangement of hexagonal cells develops with downflow in the centres (Figure 5). This flow regime has been postulated and observed by

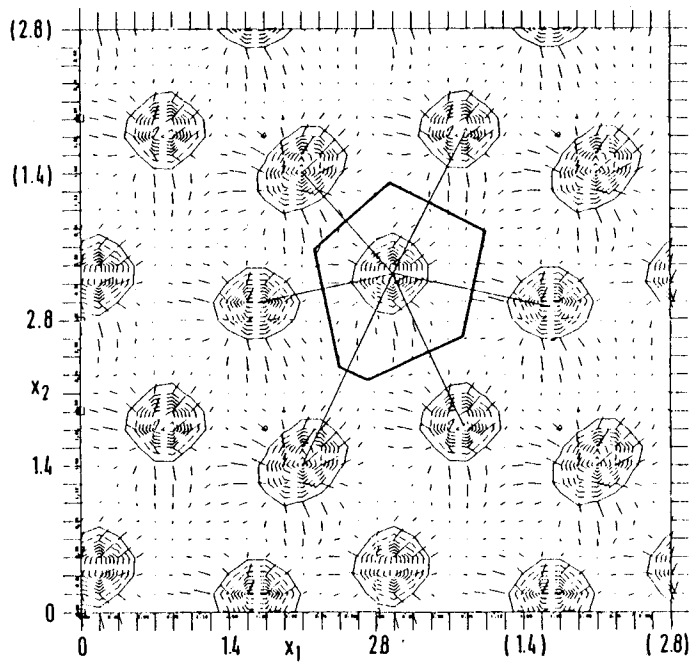

Figure 5. Horizontal section of the instantaneous velocity field at $t = 44.8$ and $x_3 = 0.188$ for $Ra = 10^5$. The isolines show the vertical velocity component, dotted lines correspond to negative velocities. $\Delta = 0.00625$ is the contour-line increment. VKM = 0.04 is the maximum vector length for the velocities in the plotting plane indicated by the magnitude and directions of the additional dashes. The figure consists of four identical plots.

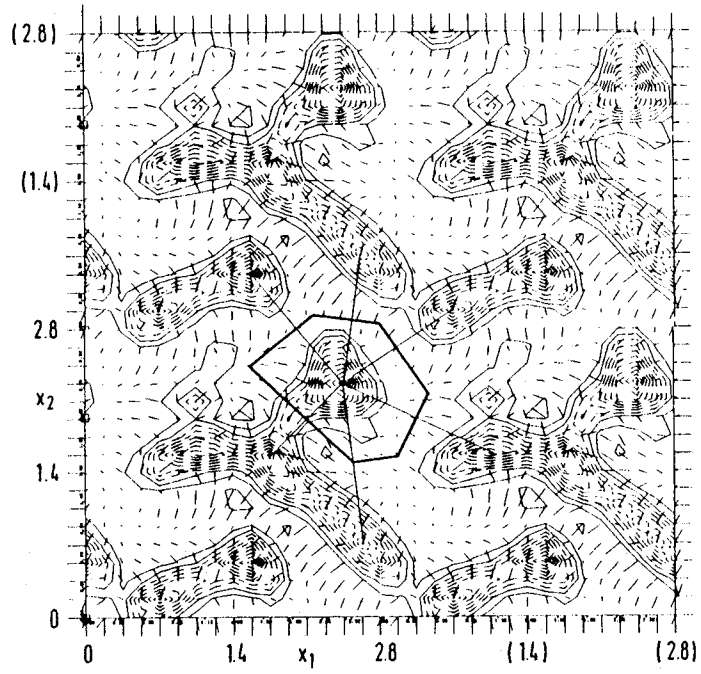

Figure 6. Horizontal section of the instantaneous velocity field at t = 75.6 and $x_3 = 0.537$ for Ra = 3.5 10^5. $\Delta = 0.025$, VKM = 0.025.

Krishnamurti [84]. Here, the cells are irregular because regular cells cannot be recorded on Cartesian grids with such short periodicity lengths. The distance λ of cell centers varies between 1.24 and 1.78 with an average value at 1.42. The flow structure calculated for $Ra = 9.4Ra_{cr}$ is a more irregular arrangement of slowly changing cells with downflow in the centers (Figure 6), as has also been observed by Kulacki and Goldstein [80]. The flow cells can still be considered to be of hexagonal form. The cells have partly grown together. The typical wavelength is between 0.75 and 1.94 with an average value at 1.29.

For $Ra = 107Ra_{cr}$ one finds time-dependent irregular structures in the horizontal sections of the temperature field given in Figure 7 and in the vertical section given in Figure 8. Vertical jets of cool surface fluid plunge from the unstable upper fluid layer downwards into the stable stratified lower fluid layer. Every newly developed jet has a tendency to merge with a close neighbor. So permanently new cells or parts of them are formed which finally contract to knots. The evaluation of other sections shows that the jets plunging downwards from the knots have the largest kinetic energy so that some of these reach the lower wall. In contrast to the jet velocities the velocity in the connecting cell or spoke structure is much smaller. Therefore the cell structure can only be found in the upper third of the channel including the upper boundary layer. The isotherm fields also show that the cold fluid in the jets interact only weakly with the surrounding hot fluid, leaving this quite isothermal. This behavior of the fully turbulent flow and the scales of the structures compare quite well with the observations by several experimentalists, e.g., by Kulacki and Goldstein [80] and Jahn [82]. The average diameter of the cells can be determined from the horizontal two-point correlations for the velocity fluctuations R_{ii} to be between $\lambda = 0.71$ and 0.85. Thus the macroscopic wavelengths found in the simulations decrease with increasing Rayleigh numbers as has been observed in all experiments.

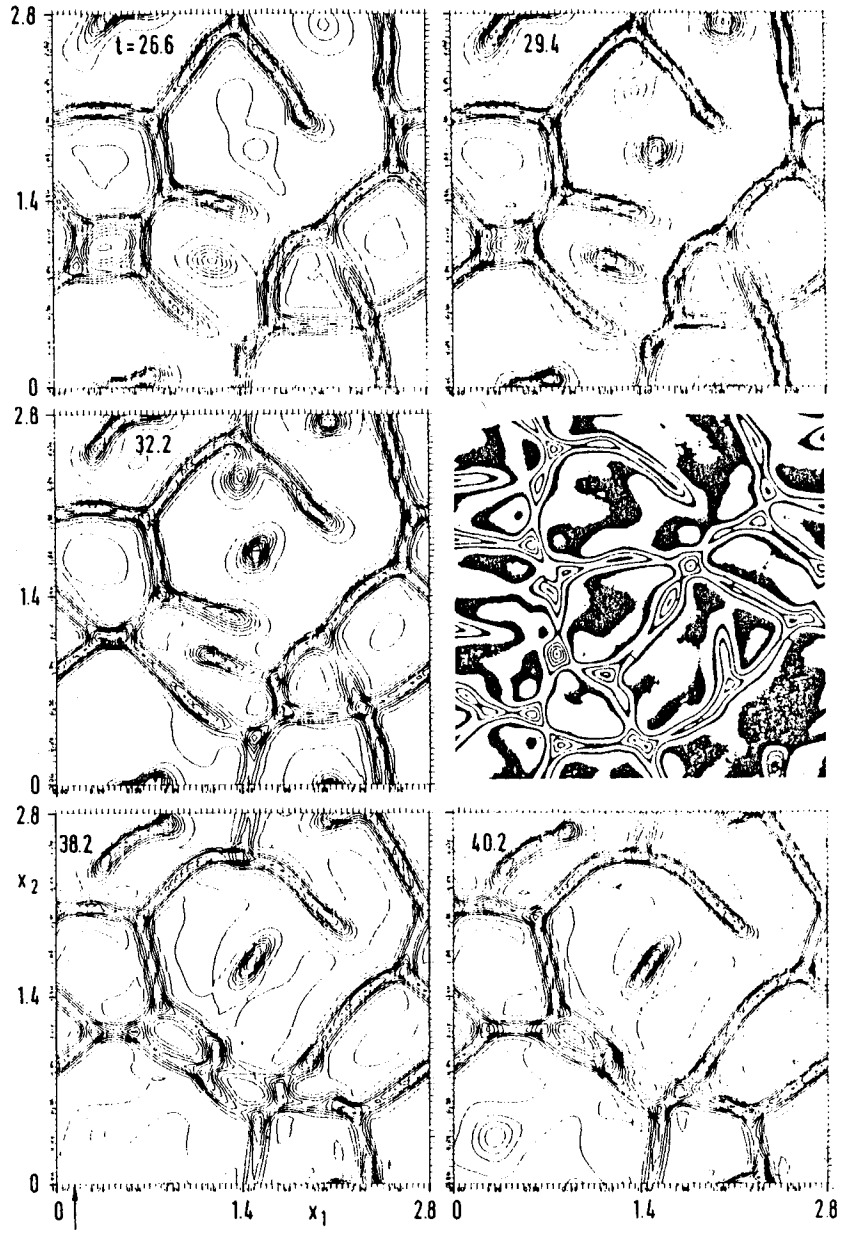

Figure 7. Horizontal sections of calculated temperature fields at several times for $Ra = 4.10^6$, $x_3 = 0.8287$ and $\Delta = 0.0625$, and an interferogram from the experiments by Jahn [82]. The arrow denotes the origin of the sections of Figure 8.

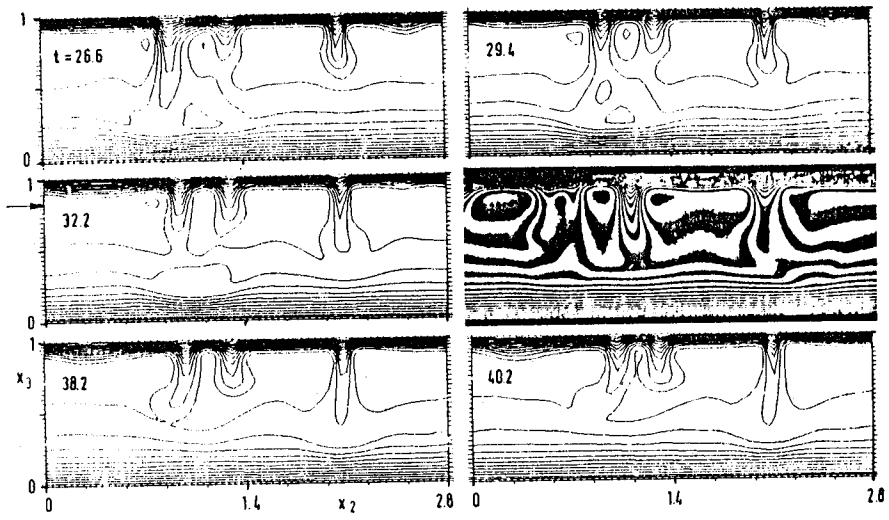

Figure 8. Vertical sections of temperature fields for Ra = 4.10^6. The arrow denotes the origin of the related sections in Figure 7. $\Delta = 0.08$. The interferogram is from the experiments by Jahn [82].

For an integral quantitative verification of the results the calculated relative amount of heat transfered downwards, η, is compared in Figure 9 to results from the literature [75, 80, 82, 85]. For fluid at rest half of the heat is transported to the lower wall and half to the upper wall. With the onset of convection η decreases because the heat transport is considerably augmented only in the upper, unstable fluid layer; the lower layer is mainly controlled by conduction. The values calculated with the TURBIT-code show no systematic deviations from the widely scattering published data. This holds also for the calculated Nusselt numbers [67].

A more detailed quantitative verification can be performed on the basis of the Damköhler number in Figure 10, which is a measure for the mean temperature maximum. The subcritical simulation gives the theoretical value for pure conduction, Da = 8. With increasing convection the Damköhler number increases as the temperature maximum is reduced from its related value for pure conduction. The calculated values are within the range of published data. The complete vertical temperature profiles for the considered cases are compared to measured profiles in Reference 68.

Thus all different kinds of available experimental data for this type of flow have been used for verification, and no dramatic deficiency of the simulations has been detected. The independence of the results on the spatial discretization has been proven in Reference 67. It has been found that a grid with $32 \cdot 32 \cdot 16$ nodes would just be sufficient to reproduce the experimental data. Therefore one should be able to evaluate other data from the simulated velocity fields, pressure, and temperature fields stored on magnetic tapes, data which have not been directly measured in this flow up to now.

Results

For a flow in a channel with infinite horizontal extension the Reynolds-time-averaging procedure reduces the set of conservation equations to the one-dimensional thermal energy equation. Models must be introduced for the unknown vertical turbulent heat flux $\langle u_3' T' \rangle$, where $'$ denotes the deviation from the local time mean value. The simplest approach is to assume gradient diffusion

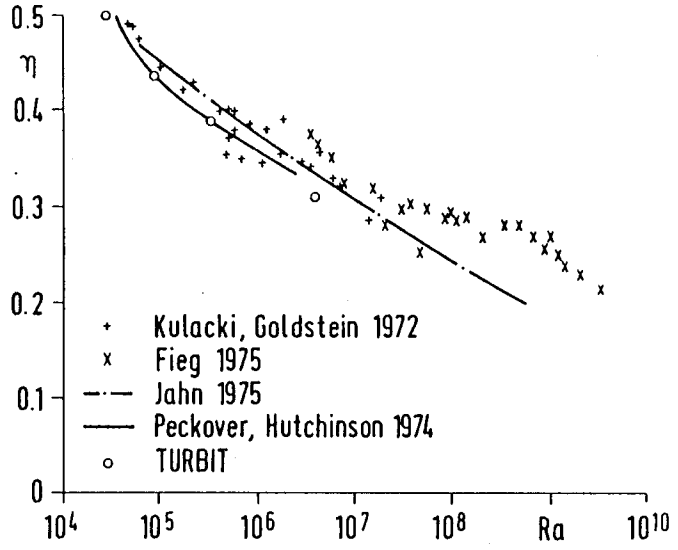

Figure 9. Relative amount of heat transfered downwards, $\eta = Nu_1/(Nu_1 + Nu_2)$.

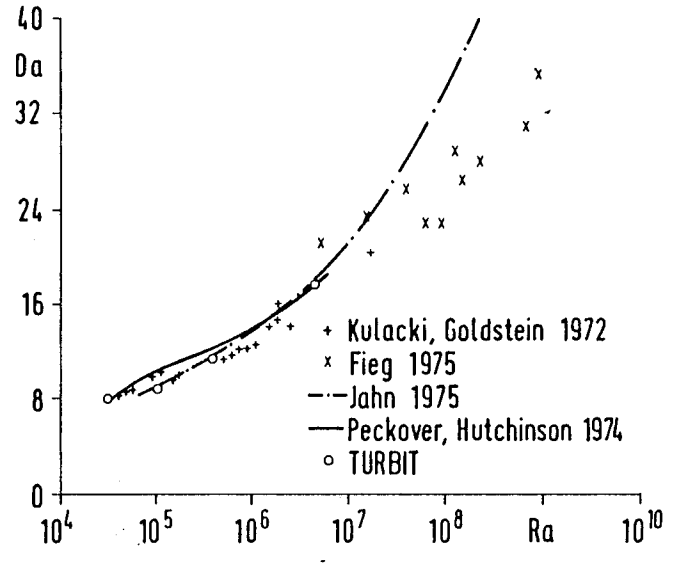

Figure 10. Comparisons of published and calculated Damköhler numbers, $Da = \hat{\dot{Q}}\hat{D}/(\hat{\lambda}\,\Delta\hat{T}_{max})$.

proportional to a local eddy conductivity:

$$\varepsilon_H = -\langle u_3' T' \rangle / (\partial \langle T \rangle / \partial x_3) \tag{59}$$

This eddy conductivity can be determined from the results of the simulations by calculating the vertical gradient of the mean temperature and the vertical heat flux $\langle {}^3\overline{u}_3' {}^v\overline{T}' \rangle$ (see Figure 11). The predicted eddy conductivity is positive near the lower and upper walls, but is negative between the plane of zero turbulent heat flux and of maximum temperature. Thus the eddy conductivity approach is no proper model in this type of flow at moderate Rayleigh numbers because it cannot account for the counter gradient heat flux.

The energy-length-scale approach has also been applied to this problem in the form of the $k - \varepsilon$ model [79]. There the eddy conductivity is approximated by:

$$\varepsilon_H \sim E^2/(\varepsilon \mathrm{Pr}_t) \tag{60}$$

Here, Pr_t is the turbulent Prandtl number. The kinetic energy and its dissipation are calculated from additional model equations. This eddy conductivity model also is not valid in the counter gradient heat flux range, but it is often used for other buoyant flows for which incomplete data exist likewise. Therefore, to support the calibration of this model for such flows, the kinetic energy and the terms of its conservation equation have been calculated (Figure 12). The energy is very

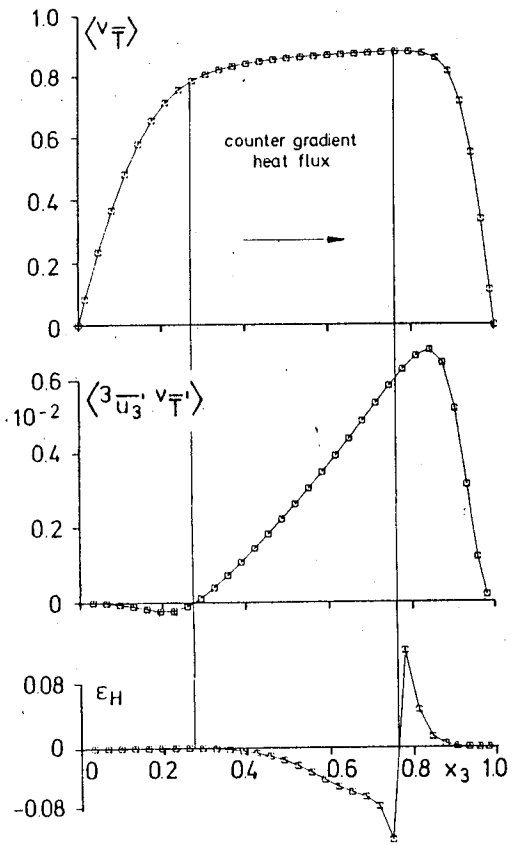

Figure 11. Counter gradient heat flux in the internally heated fluid layer; Ra = 4.10^6.

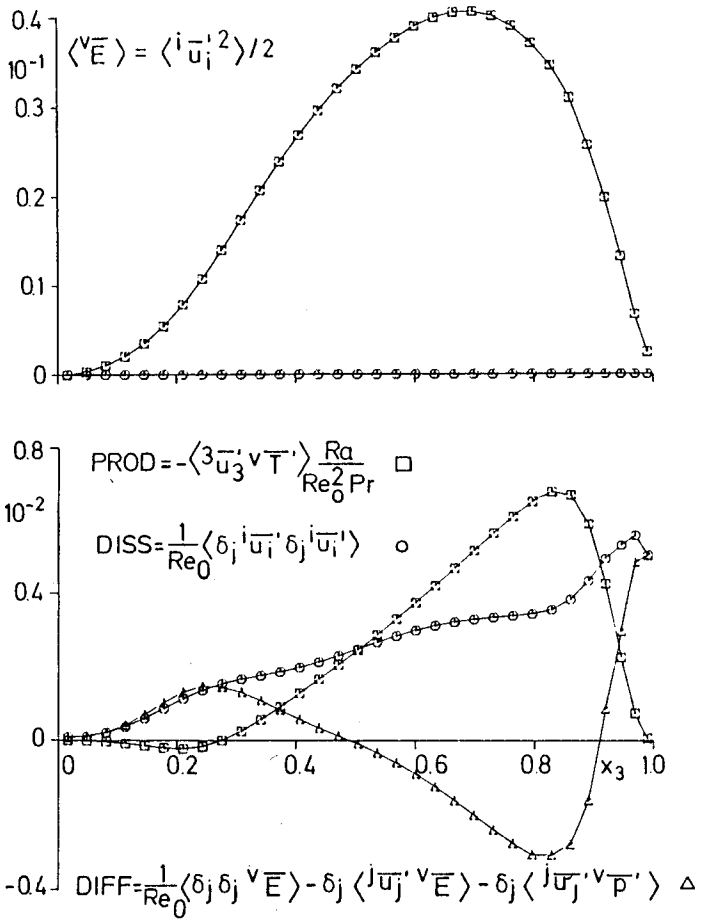

Figure 12. Vertical profiles of the calculated kinetic turbulence energy and terms of its conservation equation; Ra = 4.10^6.

small in the stable region near the lower wall. Its maximum is outside the unstable upper wall layer below the temperature maximum (Figure 11), and also below the maximum of the production term. The reason for this distribution is found from the two cross correlations contained in Figure 13, which represent the closure terms in the turbulent diffusion term. The increase of both correlations for $0.8 < x_3 < 0.9$ gives a strong negative diffusion which extracts energy. It is transported to the lower half of the channel where the turbulent diffusion is positive. The gradients of both cross correlations are comparable in size except near the walls where the pressure diffusion term predominates. The dissipation evenly increases from zero at the lower wall to a maximum value near the upper wall which can be estimated from Equation 56. In both thermal boundary layers the dissipation is approximately balanced by the diffusion term.

The most appropriate way to account for counter gradient heat fluxes would be to use models for the conservation equations of the turbulent heat flux and shear stress. Problematic terms in those equations are the pressure-scrambling terms, the pressure-diffusion terms, and the

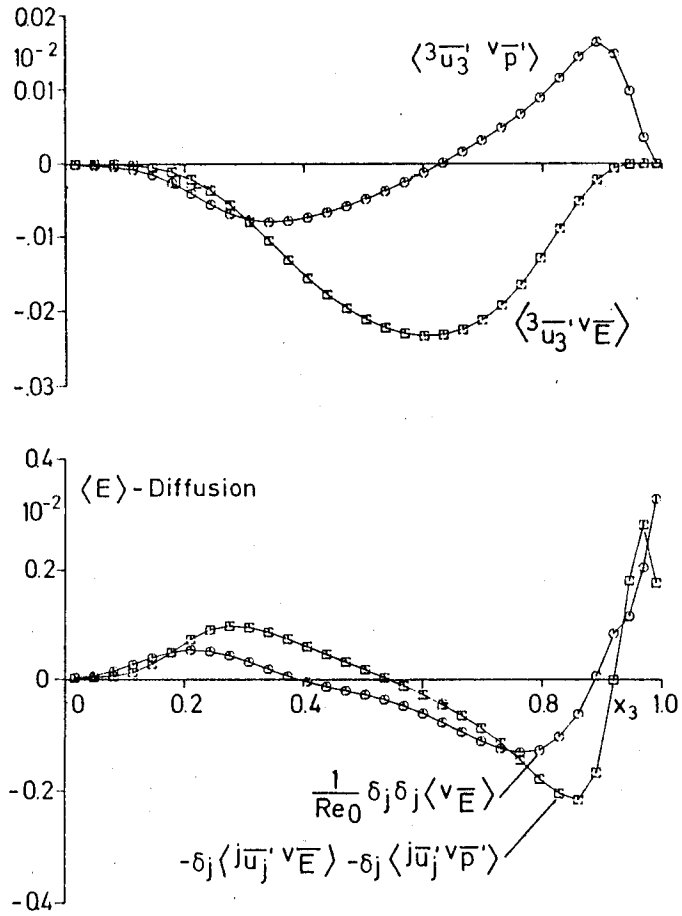

Figure 13. The closure and diffusion terms in the kinetic energy equation; Ra = 4.10^6.

pressure-strain terms for which also vertical distributions have been calculated from the numerical results [68].

The spectral distribution of the kinetic energy is investigated to support the development of models which separate some turbulence information in wave-number space like the large eddy simulation technique. The one-dimensional spectra calculated from the spatial distribution of the kinetic turbulence energy (Figure 14) are continuous in the inner third of the channel, show now distinct energy contributions, and show no extended Kolmogorov range. The Rayleigh number is too small to find the latter. At the highest wave-numbers the spectra are steeper than k^{-2}, which indicates the maximum of the dissipation according to Equation 31b, and even steeper than k^{-7}, which according to Heisenberg indicates the upper end of the dissipation spectrum.

The spectra in the upper third of the channel, mainly in the unstable boundary layer, are characterized by energy contributions in the medium and high wave-number range. The energy maximum is at a wave-number which corresponds to a wavelength $\lambda = 0.93$, or $\lambda = 0.7$ if one considers the spectra of the vertical velocity component [67]. This is approximately the average diameter

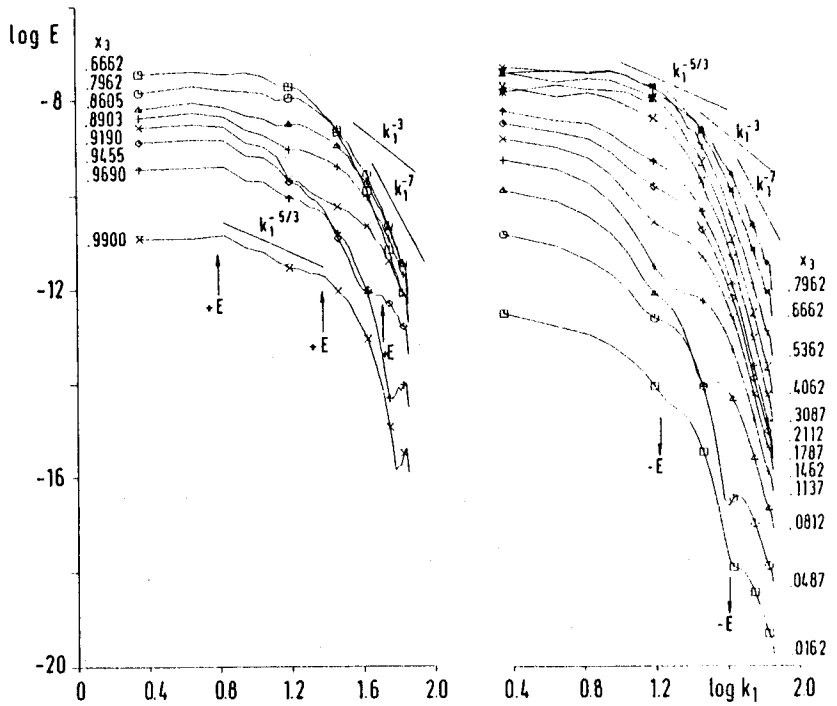

Figure 14. One-dimensional energy spectra of the spatial distribution of kinetic turbulence energy; Ra = 4.10^6; $k_1 = 2\pi/x_1$.

of the cell structures found in the isotherm fields. A second distinct energy contribution is at a wavelength of 0.35, which decreases to 0.28 in approaching the upper wall. This is the average thickness of the spoke structures and jets. Thus both bulges in the spectra are due to energy contributions by the buoyancy forces. A third bulge at the highest wave-numbers corresponds to a wavelength of 0.1. Near the wall energy may also be added due to aliasing errors. The wavelength related to this third bulge is proportional to the distance to the wall. Farther away from the wall the bulge may be absorbed by the second one. This wavelength corresponds to small-scale structures within the spoke patterns which can be detected in the isoline fields for the pressure and the vertical velocity component in the region $x_3 > 0.93$. Obviously these are the scales which are responsible for the pressure-diffusion term in the near wall range of the unstable layer, as given in Figure 13.

The spectra in the stable stratified lower third of the channel are steeper than those in the unstable layer. The down-flowing fluid has to work against the buoyancy forces extracting kinetic turbulence energy at scales which correspond to the structures in the flow field. Approaching the lower wall the large-scale structures are dumped out first. The wave-number of the energy maximum decreases because only a few of all jets penetrate the deepest layers and thus increase the distance between these jets. Nearer the wall, at about $x_3 = 0.11$, the scale of energy removal has decreased to the thickness of the jets. This thickness slightly varies with x_3 because the jets spread horizontally in the stable layer forming mushroom-like structures, as shown in Figure 8. Even closer to the wall this scale of energy removal is less distinct. It branches out forming a second more pronounced depression in the spectrum at decreasing length scales which correspond to scales observable in the fields of vertical velocity and pressure. These are related to the high energy cores of the few jets penetrating the lower wall.

The data deduced from these direct numerical simulations show that first-order statistical turbulence models using the eddy conductivity concept are no adequate tool to theoretically investigate this type of flow. Second-order models are required which have to use carefully chosen models for the closure terms. Thus the numerical expenditure of the statistical method is drastically increased by the large number of additional model equations. This gives the large eddy simulation method a chance to produce with about the same computing effort results which are less dependent on model coefficients and which are therefore more suitable to be taken as predicted data.

Turbulence Data in Liquid Metal Flows

The Problem

The turbulent heat transfer in liquid metals is of interest in those technical problems in which large heat flux densities occur. The development of liquid-metal-cooled fast-breeder reactors has considerably increased the knowledge in this field. The methods used to calculate the temperature fields in liquid-metal flows are based on the Reynolds equations requiring models for the eddy conductivities or for the turbulent Prandtl number.

Even after extensive theoretical work on eddy conductivities for liquid metal flows (e.g. [86 to 88]) there are still many open problems. Some of them are due to experimental difficulties pointed out in References 89 and 90. There are, e.g., very accurate data for mean temperature profiles for sodium flow in pipes [91], but several times it had to be concluded, e.g., in References 87 and 90, that there exist nearly no credible data on the statistics of turbulent temperature fluctuations. Such data are needed to verify or adapt some more complex theoretical eddy conductivity models like those given in References 87 and 88.

The large eddy simulation technique has been used to provide data to support these theories [21, 31, 90]. Some additional results will be given later. They demonstrate the considerable insensitivity against any changes of the model.

Case Specifications

Several nonbuoyant annular flows are considered with periodic boundary conditions in the circumferential and in the axial direction which is the direction of the mean pressure gradient $P_z = 2$ (see Figure 15). The fluid is heated at the inner wall by prescribing $q_{w1} = 1$. The outer wall is adiabatic, $q_{w2} = 0$.

The spatial resolution required for direct numerical simulations of the turbulent temperature field is deduced as earlier. The allowable mean grid width h_{max} is given by Equation 55. An approximation for the dissipation profile in turbulent channel flows follows from the assumption of equality of production and dissipation of kinetic energy. Application of the Prandtl mixing length model

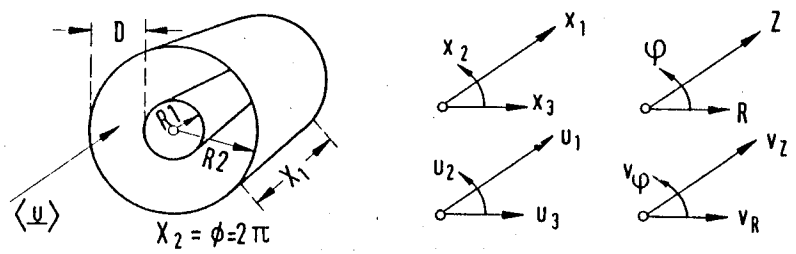

Figure 15. Geometrical specifications for pressure gradient driven liquid metal flow.

and the universal logarithmic profile furnishes:

$$\varepsilon = (\kappa y)^2 \left| \frac{\partial \langle u_1 \rangle}{\partial x_3} \right|^3 = \frac{1}{|\kappa y|} \tag{61}$$

Here, $\kappa = 0.4$ is the Karman constant, and y is the wall distance. Using the normalization procedure outlined earlier, which gives $a = 1/Pe_0$, and assuming the validity of the Blasius formulation for the friction coefficient needed in Equation 2, one gets an approximate value for the grid width required:

$$h_{max} = 19.48[|\kappa y|/(Pr\ Re^{7/8})^3]^{1/4} \tag{62}$$

A graph is given in Figure 16 for $y = 0.1$ and for the Prandtl numbers of liquid sodium, $Pr = 0.007$, and mercury, $Pr = 0.0214$. The near-wall grid width in the x_3 direction, h_{3w}, follows by discretizing the thermal boundary layers by just two nodes; this is sufficient because the temperature profile at low Peclet numbers is mainly controlled by conduction:

$$h_{3w} = D/(2Nu) \tag{63}$$

The curve for h_{3w} given in Figure 16 has been calculated using the Nusselt number correlation given by Gräber [92] for a plane channel heated at one wall using ${}^{v}\langle Pr_t \rangle = 1$.

The required periodicity lengths are chosen in accordance with the discussion of equations 37 to 39 and with the experience from Reference 21 to be $X_1 = 4$ and $X_2 = 2$. With these periodicity lengths and the maximum values for the grid width the required node numbers N_i can be determined from Equation 58 and the procedure explained in that paragraph. The results included in Figure 16 indicate that, e.g., for liquid sodium flow approximately $N_1 N_2 N_3 = 2 \cdot 1 \cdot 6$ mesh cells would be required at the critical Reynolds number to allow for direct temperature field simulations, and about $22 \cdot 11 \cdot 8$ mesh cells at a Reynolds number of 10^5.

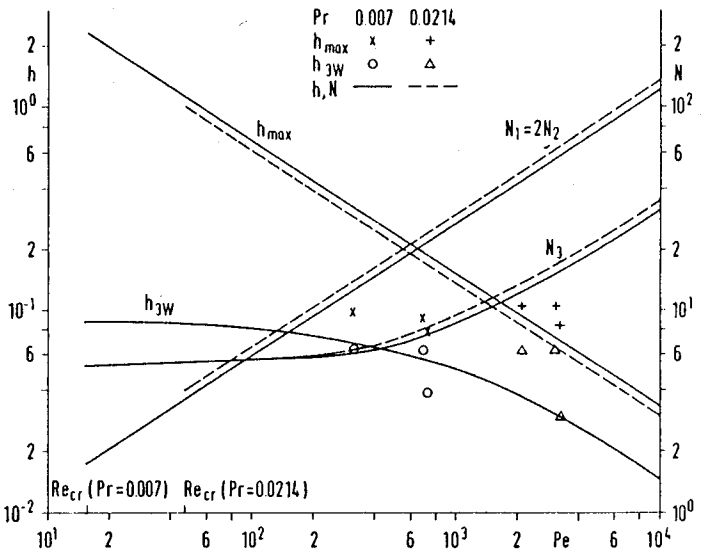

Figure 16. Grid parameters required and used for direct numerical simulations of temperature fields in liquid metal flows. The grid data are those for the nodes adjacent to the outer wall.

Table 4
Case Specifications for the Liquid Metal Flows

Pe	Pr	R_1/R_2	N_1	N_2	N_3	X_1	X_2	Δx_1	$r\,\Delta\phi_{KM}$	Δx_{3w}	$\Delta x_{3\,max}$
322	0.007	0.25	16	16	16	2	$\pi/2$	0.125	0.128	0.0625	0.0625
700	0.007	0.25	32	32	16	3.2	π	0.1	0.128	0.0625	0.0625
730*	0.007	0.25	32	32	16	3.2	π	0.1	0.129	0.038	0.068
2140	0.0214	0.479	32	32	16	3.2	π	0.1	0.185	0.0625	0.0625
3110	0.0214	0.479	32	32	16	3.2	π	0.1	0.185	0.0625	0.0625
3252*	0.0214	0.479	32	32	16	3.2	π	0.1	0.187	0.03	0.0705

* *Restarted from the preceding case with changed grid and reset of problem time.*

The requirements for direct simulations of the velocity field are shown later. There it gets obvious that none of the cases specified in Table 4 might be investigated by direct simulations even if the fastest and largest computer system available were used. On the other hand Figure 16 shows that all the grids specified for the sodium flow are sufficient to resolve all relevant scales in the temperature field. Thus one gets a combination of a large eddy simulation of the velocity and pressure field and a direct simulation of the temperature field. This result is further supported by the theory to calculate the subgrid scale coefficients which gives similar values as included in Table 1 for the subgrid scale shear stress model, but gives zero values for the coefficient C_{T2} of the subgrid scale heat flux model.

The grids used for the simulations of mercury flow are similar (Table 4). Nevertheless, due to the larger Peclet number these grids use larger mean grid widths than required as is indicated in Figure 16. Accordingly the calculated coefficient C_{T2} is greater than zero (Figure 17). The radial distribution roughly follows the dissipation profile approximated by Equation 61. For comparison

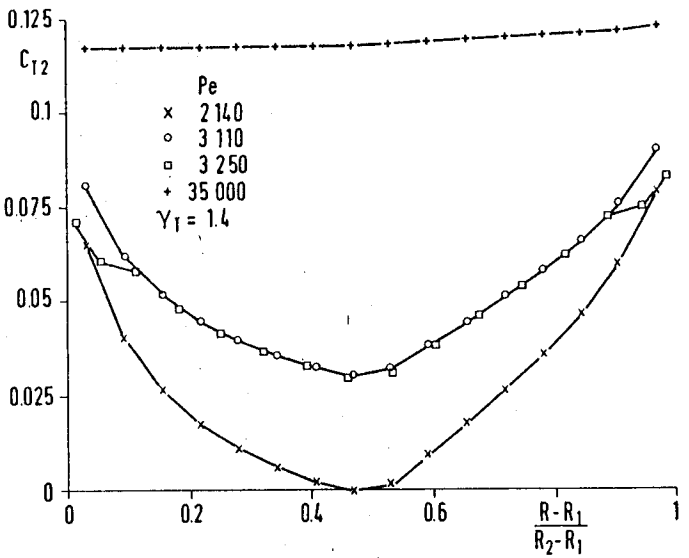

Figure 17. Radial distribution of the calculated subgrid scale coefficient C_{T2}. The coefficient is zero throughout the channel for all considered sodium flows.

the C_{T2} distribution for the air flow has been included for the example given in Table 1. The simulations of the mercury flows are in the range of transition from direct simulations to large eddy temperature field simulations. This transition follows automatically from the theory to calculate the coefficients of the isotropic model. The coefficient of the inhomogeneous heat flux model has been prescribed as recommended earlier (i.e., $C_{T10} = 0$ for the sodium flow and $C_{T10} = 1$ for the mercury flow).

As initial conditions radial mean velocity and temperature profiles are roughly approximated by logarithmic laws. Random fluctuations are superposed to these profiles and are also prescribed for the spanwise and radial velocity component. The radial distribution of the fluctuation amplitudes are approximately adapted to the expected values. Two cases have been restarted from former results as indicated in Table 4 to investigate the influence of a better resolution of the thermal boundary layers.

Verification

The time intervals of integration and of time averaging are given in Table 5. The channel lengths covered by the moving grid are for all cases greater than sixty channel widths. This is sufficient to reach fully developed flow. The computing times are also included in the table. The computing times per time step and mesh cell are larger than for direct numerical simulations because the transport equation for the subgrid scale kinetic energy takes 28% of the total computing time.

For a qualitative verification contour-line plots of the resolved instantaneous temperature fluctuations are shown in Figure 18 for two different Prandtl numbers. The isolines look random as expected for turbulent flows. The temperature fluctuations are larger near the heated wall than near the adiabatic wall. The amplitude of the fluctuations indicated by the contour-line increment Δ is larger in the mercury flow, and the location of its maximum is closer to the wall. Both sections show larger scales in the centre of the channels, whereas the scales are smaller near the walls. Thus one finds temperature fluctuations with lower wave-numbers in the inner part of the channel. This qualitative result is consistent with the importance of the temperature subgrid scale model as given by the calculated C_{T2}-distribution in Figure 17 and also with the indications of some experimental data on the macroscopic length scale [91]. In any case the dominant structures in the sodium flow are more spatially extended than the grid width which confirms that the resolution is adequate for a direct temperature field simulation. The smallest scales in the mercury flow are about of the size of the mesh cells. This indicates that the subgrid scale heat flux model really has to be used.

To obtain a quantitative over-all judgment on the simulated temperature fields the Nusselt numbers are compared in Figure 19 with empirical correlations from References 92–94. The correlation by Barthels [93] follows the numerical results at large Peclet numbers which are for liquid mercury. The numerical results for sodium flows, valid for a radius ratio of 0.25, are below most correlations. The only curve which follows all numerical results, but gives slightly lower Nusselt numbers, is the curve by Gräber [92] for a plane channel with one adiabatic wall. The results for the grids with finer resolution in the thermal boundary layers give approximately the same Nusselt

Table 5
The Time Intervals and Computing Times Used for the Simulation of Liquid Metal Flows

Pe	N_t	t_{max}	CPU-time [h]	N_{tav}	Δt_{av}
322	3,080	3.16	2/IBM 168	28	1.16
700	3,875	3.57	10.33/IBM 168	43	1.25
730	8,000	5.26	3/Siemens 7890	26	0.67
2,140	2,450	5.21	6.53/IBM 168	32	2.34
3,110	9,450	20.4	13.2 /IBM 3033	30	3.24
3,252	5,360	6.41	2/Siemens 7890	22	1.06

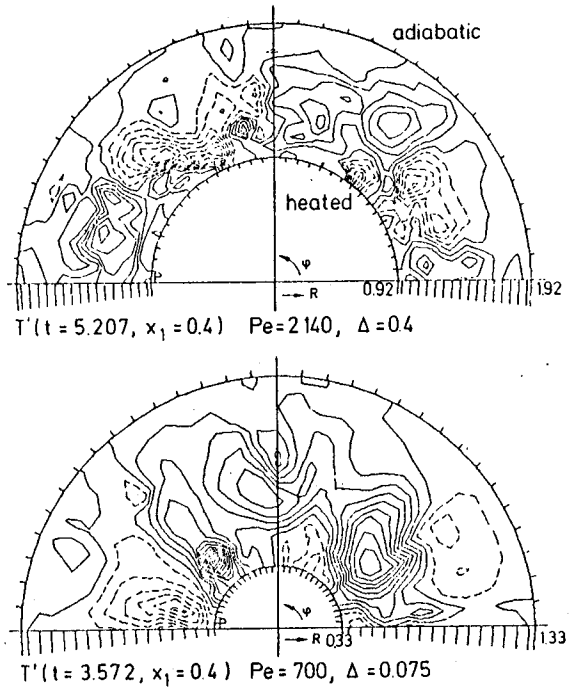

Figure 18. Instantaneous resolved temperature fluctuations ${}^{v}\bar{T}' = {}^{v}\bar{T} - \langle {}^{v}\bar{T} \rangle$ for mercury, Pr = 0.0214, and for sodium, Pr = 0.007.

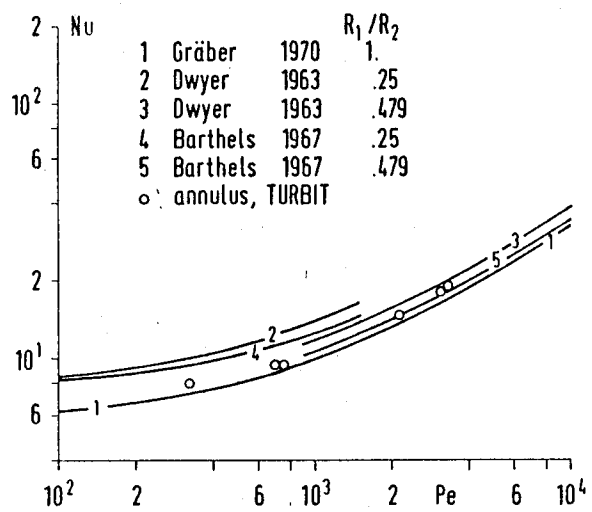

Figure 19. Nusselt numbers $Nu = (q_{conv} + q_{cond})/q_{cond}$ evaluated from simulation results and from empirical correlations.

numbers as the grids which have too-coarse mesh cells near the walls acording to Figure 16. Thus for this type of flow it is sufficient to have only one to two radial nodes in the thermal boundary layer and to use the linear wall approximations (Equations 45 and 46), for the temperature field.

A more detailed comparison of the numerical results with temperature profiles measured by Dwyer et al. [95] is made in Figure 20. The temperature profiles are nearly identical. Due to the somewhat higher Reynolds number the numerical results for the eddy conductivity are higher than the original and the smoothed data calculated from the measured temperature profile by Dwyer et al. The typical standard deviations indicate comparable uncertainties in the numerical and experimental results. Further calculated eddy conductivities for other Peclet numbers have been used in Reference 31 for comparisons to experimental data to verify the subgrid scale heat flux model.

Some problems might arise in simulating liquid-metal flows due to the departure of the temperature fluctuation spectra from the Batchelor spectrum (Equation 10 and Figure 1) and due to the missing dependence of the damping function f_H (Equation 19b) on the Prandtl number. These problems have been investigated in a sensitivity study [31] within the transition range of the subgrid scale heat flux model. Almost no influence on the numerical results could be detected, although, e.g., γ_1 has been changed from one to one hundred. The uncertainties in the model coefficients are obviously of no importance in cases in which the spatial resolution approaches the bound of total resolution. This has also been found in the verification procedure for the subgrid scale shear stress

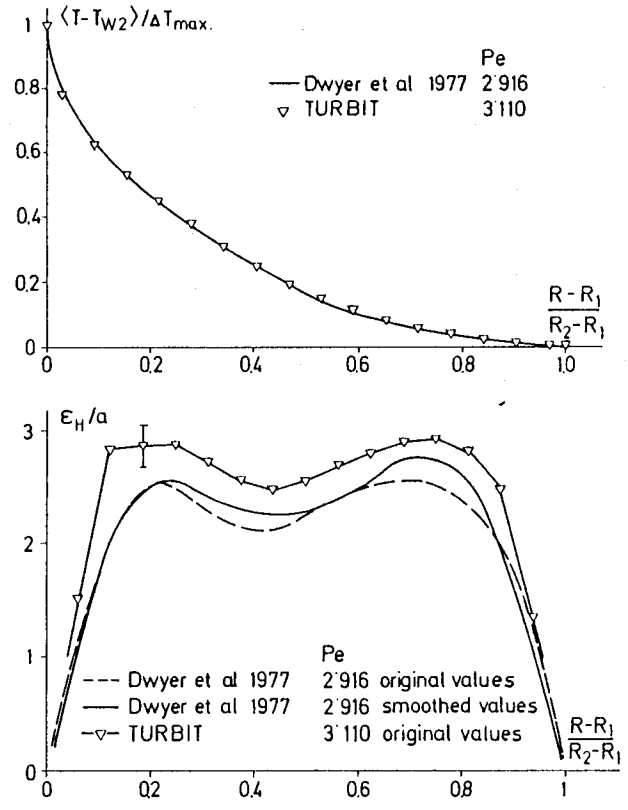

Figure 20. Calculated temperature and eddy conductivity profiles compared to measured and deduced annular flow data.

model at low Reynolds numbers [21, 41]. Thus there remains no meaningful way to adjust any correction coefficient in these liquid-metal flows to account for deviations from measured data which might occur.

Results

Information on the spatial and spectral distribution of turbulent temperature fluctuations can be used to predict turbulent Prandtl numbers and to support advanced statistical turbulence models using transport equations for some turbulence quantities. For example Lawn [87] developed a spectral theory to predict temperature fluctuations in liquid metals. When he tried to check this theory by summarizing experimental data for the turbulent Prandtl number, for the turbulent heat flux, for the root-mean-square (RMS) value of temperature fluctuations and cross stream velocity fluctuations, and for the heat flux correlation coefficients, he had to conclude that many of the published data are in error because they show correlation coefficients greater than one.

Calculated and measured peaks of the radial temperature RMS value profiles are plotted in Figure 21. At medium and low Peclet numbers the RMS values strongly depend on the Peclet number. Further influences arise from the radius ratio and from the thermal boundary conditions. The experimental results for pipe flows scatter widely. The main reason for the scatter has been postulated on the basis of the first simulation results to be due to the limited frequency range of the sensors and electric equipment used [90]. Meanwhile, the experimental data by Bunschi [99] confirm this prediction. He concluded that the temperature RMS-values found by Fuchs should be higher by at least 30% due to the high frequency cutoff used in these experiments. This discussion

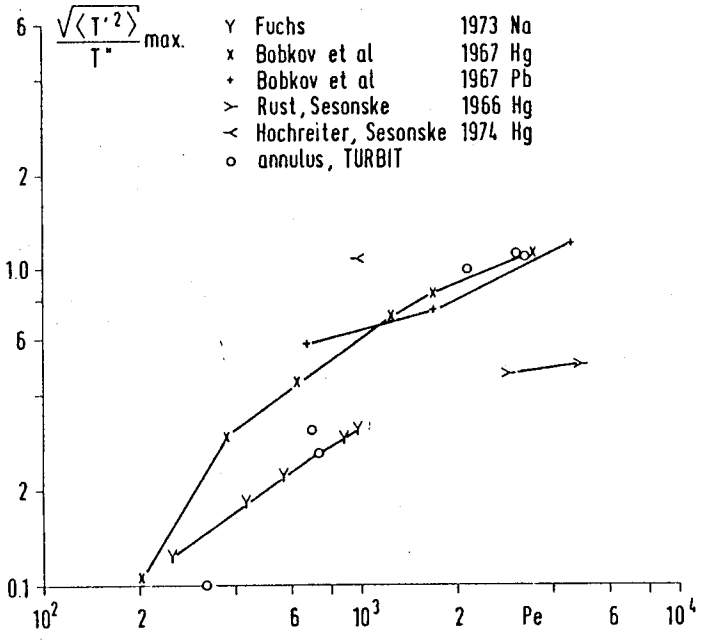

Figure 21. The peaks of the radial temperature RMS-value profiles. The experimental data by [91, 96, to 98] are for pipes.

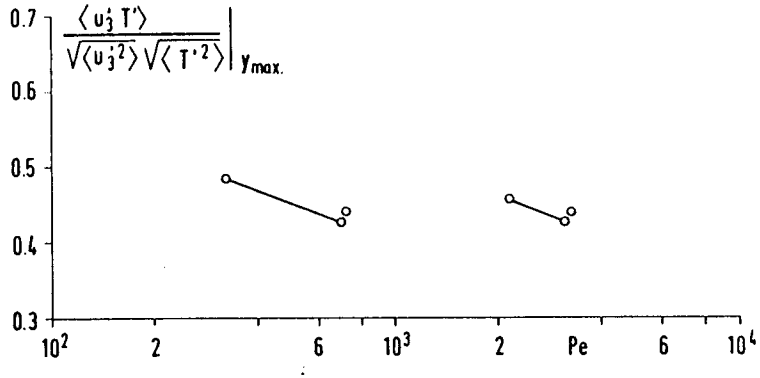

Figure 22. Dependence of resolved radial heat flux correlation coefficient on the Peclet number at position y_{max} of the maximum of the RMS temperature values.

indicates why Lawn could not verify his calculated correlation coefficients: They contain the uncertain RMS temperature fluctuations.

The calculated correlation coefficients gathered in Figure 22 are around 0.45. They show a uniform decrease for each Prandtl number with increasing Peclet number. This is mainly due to volume averaging of the basic equations. The values calculated for other Peclet numbers and for Prandtl numbers around one are about the same. Thus the numerical data confirm the results of Lawn's theory that the heat flux correlation coefficient is, if at all, a weak function of the Peclet number, except for very low Peclet numbers with $\varepsilon_{11}/a < 1$ for which the convective heat flux is insignificant compared to the pure conductive heat flux.

The "pressure scrambling" terms $\langle p' \partial T'/\partial x_j\rangle$ appearing in the transport equations for the turbulent mean heat fluxes have to the knowledge of the author not yet been determined directly from experiments. These can easily be calculated from the numerical results (Figure 23). The curve for $j = 1$ is an approximate mirror image of the curve for $\langle p'T'\rangle$ given in Reference 100. In the middle of the channel positive values are obtained for $j = 3$. Elsewhere the result is negative. This overswing has also been observed for other Prandtl numbers (e.g. for air [21]) and for other types of flows, (e.g., Rayleigh-Bénard convection [101]).

The overswing is not described by the model of Launder [102] for homogeneous flows:

$$\left\langle p' \frac{\partial T'}{\partial x_j}\right\rangle = -C_{1T}\frac{\varepsilon}{E}\langle u_j' T'\rangle + C_{2T}\langle u_i' T'\rangle \frac{\partial \langle u_j\rangle}{\partial x_i} \tag{64}$$

Therefore the model coefficient C_{1T} is not constant for the inhomogeneous flow which occurs here (Figure 23). Only in the region near the outer wall, where the temperature profile is almost homogeneous (see Figure 20), does C_{1T} exhibit a small range with approximately constant values. This range completely vanishes if both walls are heated or cooled, as shown in Figure 24 for a symmetrically cooled plane channel. Therefore, the first term of Equation 64 is not adequate for inhomogeneous flows. The second term can apparently be applied to inhomogeneous flows because of the smooth curve for C_{2T} in both channels. The value $C_{2T} = 0.5$ estimated by Launder is approximately confirmed by the simulations results, and the estimated value $C_{1T} = 3.2$ is also found to be valid for homogeneous temperature fields.

The results of these combined large eddy and direct simulations of liquid-metal flows demonstrate the capabilities of the method. The calculation of the model coefficients depending on local grid and flow variables turns out to be the basis for simulations in the range between pure direct and pure large eddy simulations.

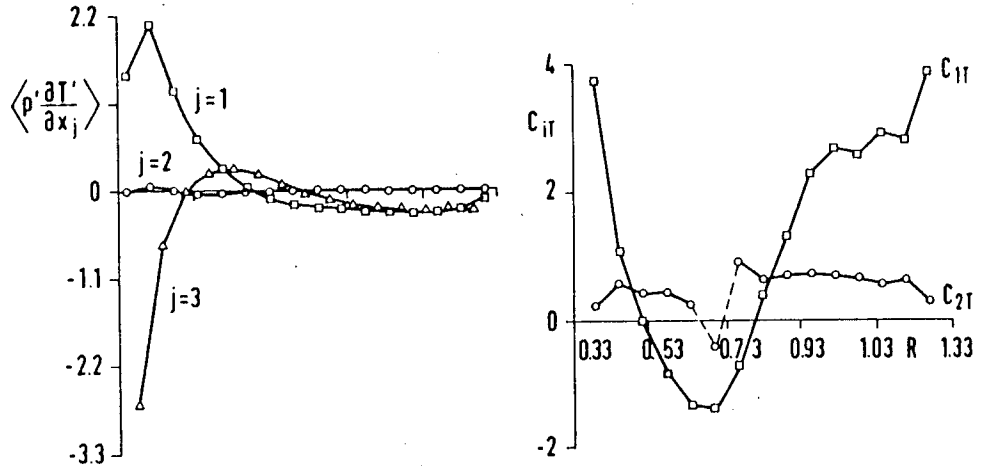

Figure 23. The predicted pressure scrambling term and the coefficients for the model by Launder. Annular flow of sodium with Pe = 700 and an adiabatic outer wall.

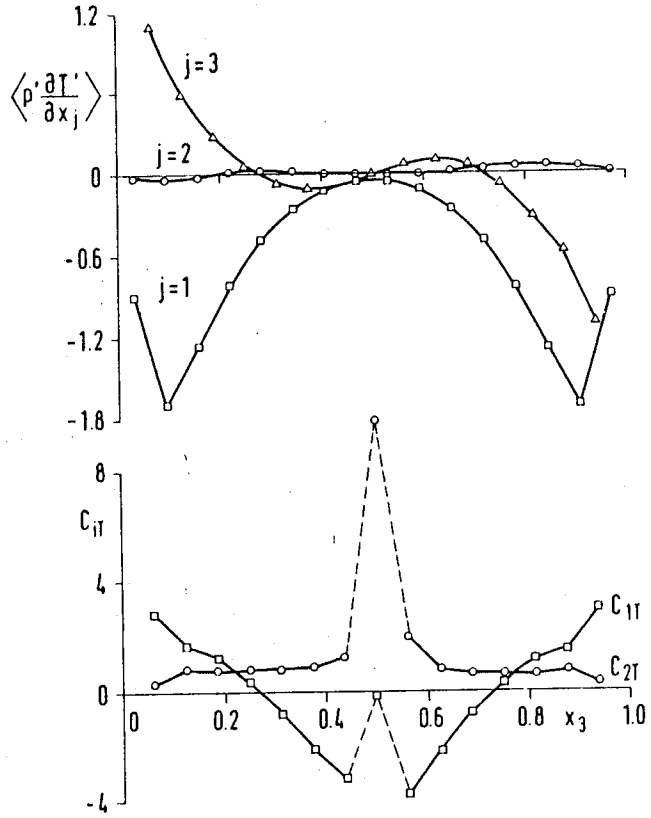

Figure 24. As Figure 23, but for a sodium flow with Pe = 350 in a symmetrically cooled plane channel. (The detailed specifications are given in Reference 31.)

Thermal Mixing in Buoyant Vertical Channel Flow

The Problem

At the HDR nuclear reactor at Kahl (Fed. Rep. Germany), blowdown experiments have been performed to study the fluid- and structure-dynamical loadings on the reactor vessel and its internals for a sudden depressurization. It was intended to use an initial temperature distribution within the vessel, which is typical for a water-cooled nuclear reactor during normal operation. To initialize such a temperature distribution it was foreseen to feed the pressure vessel with two mass flows of different temperatures, a hot water flow $\dot{m}_h$ to the upper plenum and a cooler one $\dot{m}_c$ to the lower plenum, and to remove both flows through the downcomer (Figure 25).

In planning these experiments it was feared that in case of an insufficient mixing of both flows in the lower plenum and in the annulus secondary currents or a "chimney" of hot fluid would be produced by the immense buoyancy influences which might lead to nonuniform initial temperature distributions. To investigate the mixing in the downcomer, large eddy simulations have been performed with the TURBIT code [35]. This theoretical method was the only available one for the predictions.

Case Specifications

With the available computers in 1977 it was not feasible to treat the total length $L \approx 50D$ of the annular space of the downcomer. Therefore, and due to the general problem of specifying turbulent inlet and outlet conditions, we restricted ourselves to a crude approximation and used a

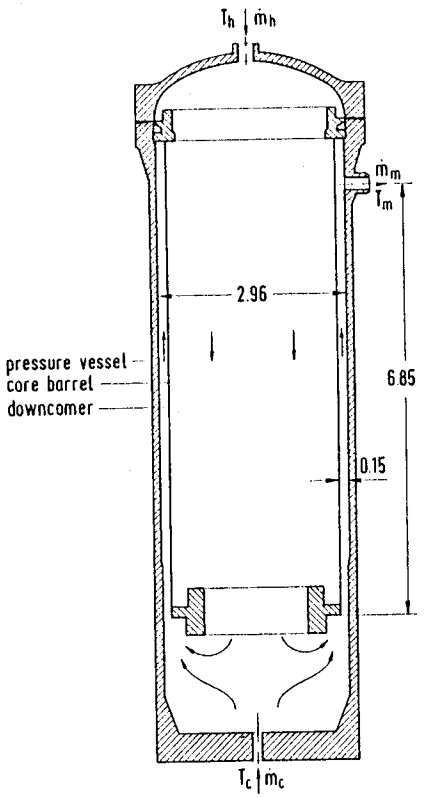

Figure 25. Flow paths within the HDR-reactor in setting initial conditions for blowdown experiments. The flow parameters in the downcomer are Re = 144, 880, $Gr_{01} = \hat{g}\hat{\beta}\,\Delta\hat{T}_w\hat{D}^3/\hat{\nu}^2 = -2.3 \cdot 10^{10}$, Pr = 0.89.

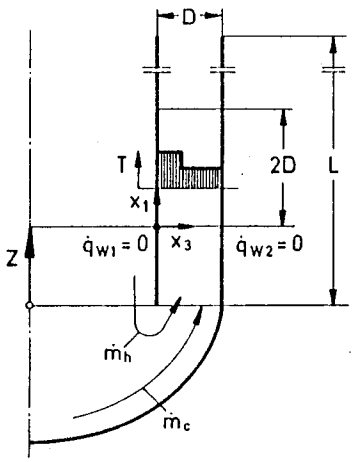

Figure 26. Model specifications for the downcomer problem. The moving control volume is temporarily at a distance Z from the downcomer inlet.

small control volume with periodic boundary conditions moving with the bulk velocity (Figure 26). Thus the small axial gradients within the adiabatic annulus are not included, but one gets a rather realistic approximation with tolerable computing times.

According to Reference 50 the grids required for direct simulations with linear wall approximations for flows with $Pr > 0.59$ follow from the requirements for the temperature field (Equations 55, 57, 61). For this special example, however, there are no thermal boundary layers in the adiabatic system to estimate h_{3w}. Therefore the resolution criteria for the velocity field are applied instead. From the procedure given in Reference 50 a suitable mean grid width h_{max} is deduced from the subgrid scale coefficient C_2, (Equation 30a), which must be zero for direct simulations. For an isotropic grid the numerator reduces to:

$$h \leq h_{max} = 5.13(\nu^3/\varepsilon)^{1/4} \tag{65}$$

Using the dissipation given in Equation 61 and the Blasius formulation for the friction coefficient we get:

$$h_{max} = 28.97[|\kappa y|/Re^{21/8}]^{1/4} \tag{66}$$

This equation evaluated for $y = 0.1$ in Figure 27 meets all requirements formulated by Chapman [10] for resolving relevant turbulence structures such as bursts, etc. A grid width in the x_3 direction, h_{3w}, suitable for linear wall approximations follows from the assumption that the viscous sublayer has to be discretized by three nodes. The thickness of the sublayer is $y^+ = \hat{y}\hat{u}_0/\hat{\nu} = y\,Re_0 = 5$. By use of Equation 2 and the Blasius law one gets:

$$h_{3w} = 16.7Re^{-7/8} \tag{67}$$

Desirable periodicity lengths are the same as for liquid-metal flows, $X_1 = 4$ and $X_2 = 2$. For these values, the required node numbers N_i can be determined from Equation 58 and the Δx_3 doubling procedure explained in that paragraph. The results included in Figure 27 indicate that approximately $49 \cdot 25 \cdot 15$ mesh cells would be required for direct velocity field simulations at the critical Reynolds number, and about $770 \cdot 385 \cdot 200$ mesh cells for the Reynolds number of the HDR problem, $Re = 144{,}880$. The upper bound for tolerable direct simulations to be performed on the latest computers may be reached at $Re \approx 2 \cdot 10^4$ because such simulations would require $205 \cdot 103 \cdot 56$ mesh cells.

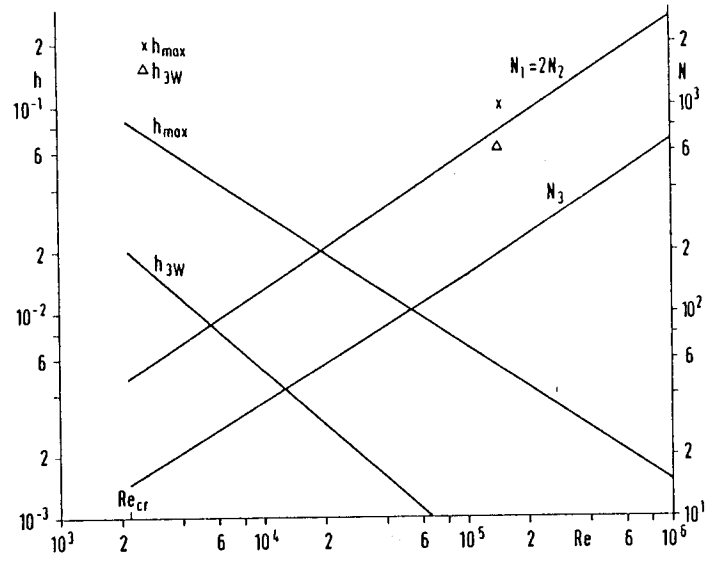

Figure 27. Grid parameters required for direct simulations of the velocity field in forced channel flows and used with the large eddy simulation of the HDR problem.

The grid actually used is very coarse with $N_1N_2N_3 = 16 \cdot 8 \cdot 16$ nodes and $X_1 = 2$, $X_2 = 1$. The corresponding grid widths included in Figure 27 are one to two orders of magnitudes above the requirements for direct simulations, which means that subgrid scale models and wall functions for the boundary conditions of the velocity field have to be used. The influence of buoyancy on the wall functions is neglected.

In the initial conditions no mixing of the two mass flows is assumed in the lower plenum. This leads to a step change in the radial mean temperature profile at the entrance of the downcomer (Figure 26) and to zero initial turbulent heat fluxes. For this reason random temperature fluctuations are superimposed, whereas the velocity field is assumed to be fully developed and is taken from former calculations of nonbuoyant flow with the same grid. The normalization of the variables is as in the earlier sections. The Reynolds number Re_0 is kept constant, $Re_0 = 3{,}300$. The wall temperature difference ΔT_w at the entrance is used as a temperature scale.

To study the influence of the buoyancy forces two cases are considered. In the first simulation with Grashof number $Gr_{01} = 0$ no buoyancy forces are included, and in the second one with $Gr_{01} = -2.27\ 10^{10}$ the buoyancy forces are included.

Verification

For both cases the complete large-eddy simulation scheme has been integrated in time until the control volume has been transported over the axial distances Z_{max} indicated in Table 6. The corresponding CPU-times on an IBM 370/168 are 18 and 45 minutes, respectively. On the recently available Siemens 7890 these simulations would require only 2.5 and 6.3 minutes. To evaluate the spatial distribution of velocity and temperature profiles in the downcomer, mean values have been taken over the planes parallel to the walls at certain time steps. For this purpose the physical velocities are used and not the values transformed by a Galilei transformation.

A direct verification of the results cannot be performed because to the knowledge of the author there exist no directly applicable data in the literature. Therefore a verification can only be done

Table 6
The Number of Time Steps, Computing Times, and Final Results of the Large Eddy Simulations for the HDR Problem

Gr_{01}	N_t	CPU-time [min]	Z_{max}	ΔT_w (Z_{max})	Gr (Z_{max})
0	1020	18.3/IBM 168	50.4	0.285	0
$-2.27 \cdot 10^{10}$	2280	44.3/IBM 168	32.4	0.0005	$-1.1 \cdot 10^{7}$

by analogy considerations, for example on the basis of the decay laws for the wall temperature difference along the annulus, (Figure 28). When buoyancy is neglected the temperature difference decreases proportional to Z^{-m} with m = 0.7. This value is between those for plane jets with m = 0.5 and round jets with m = 1 [103], and it is near m = 0.8 for the adiabatic wall effectiveness in turbulent boundary layers with slot injection [104] which gives the more relevant comparison. With buoyancy a steeper decrease is found with different power laws in different regions. The power law found at small values of Z is related to the region in which the mixing layer reaches the hot wall. The other power law is found at larger Z values where the temperature decrease is steeper. There the mixing layer also extends to the cold wall. The exponent m = 1.38 for the first region is again between m = 1 for plane and m = 5/3 for round buoyant jets [103]. From this qualitative agreement one may conclude that no markable deficiencies arise from the application of the theory for stationary isotropic turbulence given earlier to calculate the coefficients for the time-dependent model.

A further problem may arise from the choice of the boundary conditions which do not include any influence of buoyancy on the logarithmic laws of the wall. This problem is investigated by comparison of the axial distribution of the calculated friction factor to the values from the correlation by Petukhov [105] (Figure 29). The calculated distribution is somewhat irregular due to statistical errors and due to some effects discussed in the next section. For small values of Z the empirical curve deduced on the basis of local flow parameters is above the calculated results because it takes some time to develop the larger turbulence caused by the large buoyancy forces at the entrance of

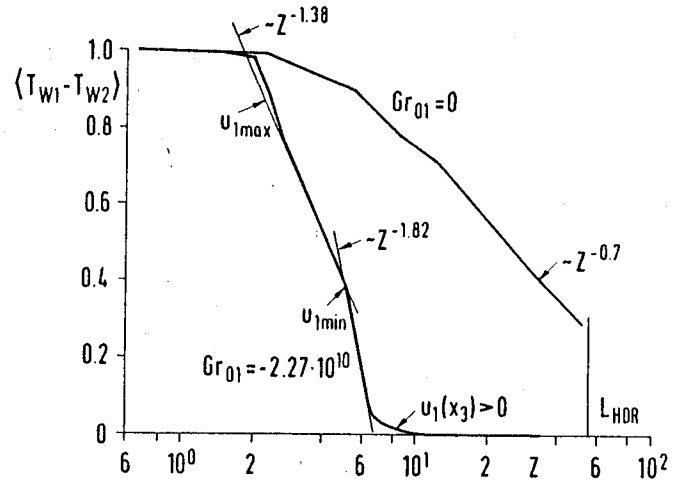

Figure 28. Axial decay of the wall temperature difference in the downcomer.

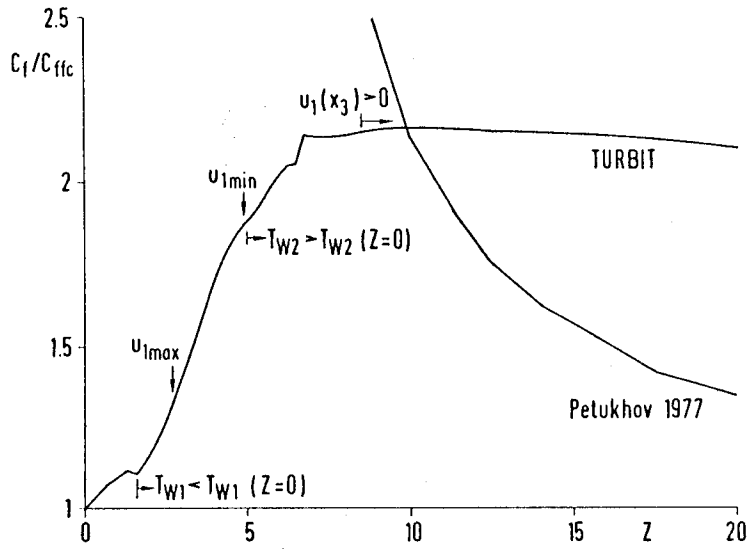

Figure 29. Axial distribution of the calculated local friction factor, C_f, divided by the one for pure forced convection, C_{ffc}, compared to the locally applied formula by Petukhov for fully developed flow.

the downcomer. For large values of Z the correlation for fully developed flows is below the simulation result because the buoyancy forces in the HDR problem are reduced, and thus the turbulence level also decreases. Both curves intersect just at the position of the calculated maximum value. This coincidence of the positions of equality of the friction factors and of the calculated maximum confirms that turbulence production is mainly by buoyancy forces within the core of the flow and not by shear near the wall. Thus the wall approximations are adequate to this problem.

Results

Some of the predicted radial velocity and temperature profiles for the buoyant flow are given in Figure 30. For Z > 0 the hot fluid accelerates, reaching its local maximum value at Z = 2.7 where the mixing layer in the temperature field reaches the hot wall, and decelerates for larger Z. The cold fluid accelerates in the negative Z direction. The maximum of recirculation occurs at Z = 5 where the temperature mixing layer reaches the cold wall. The flow decelerates for larger Z. At Z = 9 the velocity is again positive all over the channel and no relevant temperature differences remain.

The fast radial mixing is caused by a rapid production of turbulence at the mixing front. For example Figure 31 shows a fast build up of large temperature fluctuations and large radial turbulent heat fluxes. The velocity fluctuations and the shear stresses behave in a similar manner, so that the initially developed flow reversal is suppressed not too far from the entrance. Therefore no extended hot chimney or secondary currents can develop. On the contrary the radial temperature differences have disappeared already below half of the length of the adiabatic channel (Table 6 and Figure 28), so that buoyancy contributions to the driving pressure gradient are negligible for the upper half of the channel.

Thus in the investigated case the buoyancy forces make the down-stream flow distribution within the downcomer inherently stable against nonuniformities in the temperature field at the entrance.

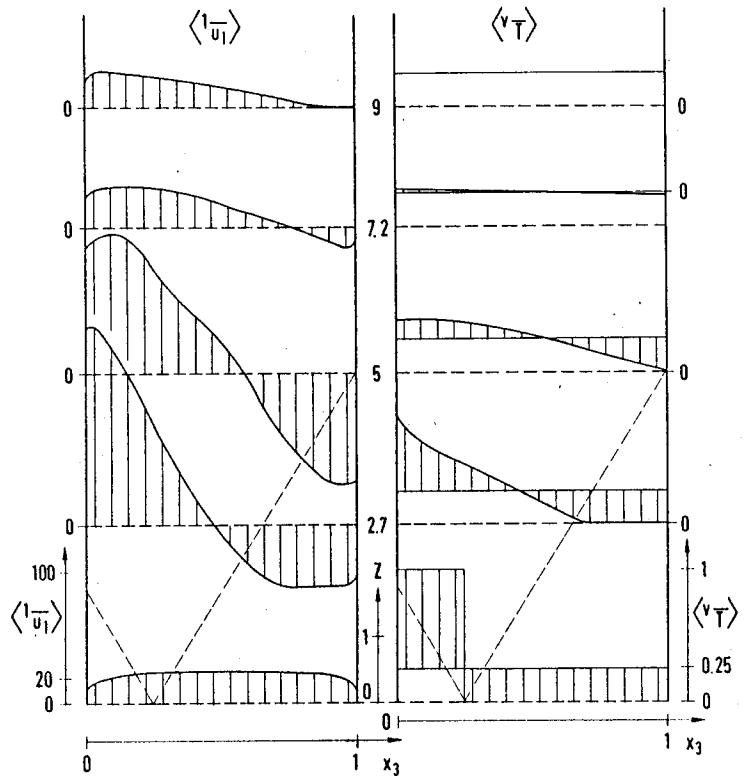

Figure 30. Predicted radial velocity and temperature profiles within the lower nine channel widths in the downcomer. $Gr_{01} = -2.27 \cdot 10^{10}$.

Therefore no serious difficulties had to be expected with the chosen experimental method for providing initial temperature fields suitable for blowdown experiments in the HDR reactor.

After having finished this theoretical investigation, measurements of the temperature field had been performed in the HDR reactor which are in accordance with the conclusions to this theoretical prediction [106].

CONCLUSIONS AND OUTLOOK

In numerical simulations of incompressible turbulent channel flows mainly finite difference schemes are used. They are easy to understand, easy to program, and easy to handle in case of computer code modifications. The accuracy of finite difference schemes is sufficient for most simulations because the physical flow phenomena to be investigated anyway require very fine spatial resolution. The only field in which spectral schemes are preferably used is the investigation of the laminar to turbulent transition in pressure-driven channel flows. The finite-difference scheme applied here follows from a formal volume-integration procedure. This gives clear definitions not only for the flow field variables but also for the definition of the unknown closure terms, the subgrid scale terms, especially in anisotropic grids.

The method of direct numerical simulation results from the volume integration procedure by neglecting the subgrid scale terms and applying linear wall approximations. Thus in this numerical

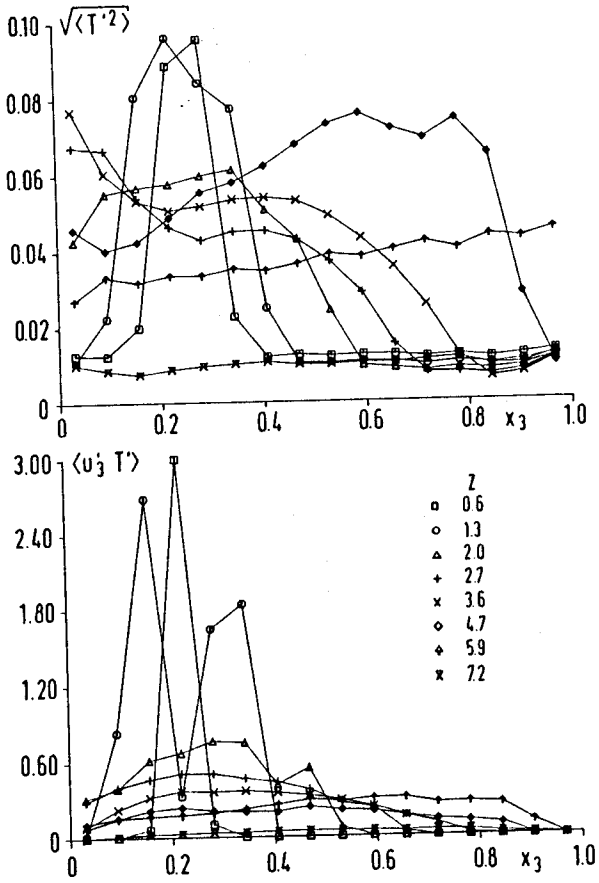

Figure 31. Radial profiles of the temperature fluctuations and the radial turbulent heat flux. $Gr_{01} = -2.27 \cdot 10^{10}$.

scheme no model coefficients are used. It is the only available universal turbulence model. It can strictly be used for predictions of any type of flow. The only requirement for application of the method is the demand for very fine grids which resolve all relevant scales of turbulence. On present computer systems this restricts the applicability to flows with moderate turbulence levels. As a reward for the large computation times one gets all flow field variables for each mesh cell and each time step. From the flow fields any statistical data, like autocorrelations, two-point correlations, cross correlations, etc. can be computed. Accordingly the results of the TURBIT code given for an internally heated horizontal convection layer indicate the main fields of applications. These are the investigation of flow structures and turbulence phenomena and the calculation of statistical data of turbulence, some of which cannot be determined by experiments up to now, to support the development of empirical models. Direct simulations of fully turbulent pressure-driven flows have not yet been published. Nevertheless, the estimation of the grids required for a Reynolds number of about 10^4 are with $128 \cdot 64 \cdot 37$ mesh cells within the capabilities of our available computer systems.

They would require about 35 hours of computation time on a common Siemens 7890. Thus we can now expect such simulations which should help us to get a better understanding of turbulence.*

The method of large eddy simulation directly describes the large-scale part of turbulence. The small-scale part is modeled by subgrid scale assumptions. This method is fairly universal and therefore also capable for predictions when fine grids are used. For coarse grids the computation times are drastically reduced, but the empirical input to the model has to be increased. In any case, the sensitivity of simulation results against model coefficients is very low for the subgrid scale model used here, because nearly all model coefficients are determined theoretically by means of Kolmogorov's energy spectra. This theory, which accounts for local grid and flow parameters, gives a continuous transition from direct simulations to large eddy simulations if the grid size or the Reynolds number is increased. The simulation results given here indicate that without this feature one would not be able to predict the turbulent temperature fields for low Prandtl number flows. Especially this application shows that the large eddy simulation technique cannot only be used to study large-scale phenomena in turbulence but also to supplement experimental data.

There are some problems which hinder extended applications of the method in the future. Both types of simulations need specification of turbulent inlet and outlet conditions. To use periodic boundary conditions with a moving grid is a tolerable approximation only for few flows. A solution may come from decoupling the intended simulation from the specified inlet and outlet conditions by interposing additional coarse grid simulations on both sides of the flow area to be considered. The wall approximations used in large eddy simulations for high Reynolds number flow should be improved and generalized. This would considerably increase the chance for the method to be applied to engineering problems in the near future. Some more general problems are those of code verification. This can hardly be performed because such codes provide an obviously quasi random output. The usual checks must therefore be to investigate three-dimensional laminar flow problems, to investigate the structures in turbulent flow fields, and to compare as many different statistical data to experimental data as possible. Of course, there will remain some deviations which may be due to deficiencies of the spatial resolution, of the numerical model, or of the experimental data. Thus it will remain a hard job to show that the results are credible.

In the near future the applications of both methods still will be in the fields already mentioned. In addition the large eddy simulation method will surely be applied to engineering problems. It can already now serve as a tool to investigate prototypical engineering problems for which no other tested empirical models or experimental data are available. The results given for a strongly buoyancy-influenced vertical channel flow simulated on a coarse grid show that the method can effectively be used instead of complicated and expensive experiments to clarify qualitative key questions. Some other problems the method is destined for are investigations of flows in which the fluctuating field variables are of direct interest. Such problems are for example the aerodynamic noise generation, the fluid structure interaction in naval research, or the alternating tensile stresses due to thermal stresses in large containers and pipe systems in nuclear reactor research.

Finally, one may expect that within the next decade the large eddy simulation method will partly take the place of the Reynolds models, especially as regards the calculation of complex two-dimensional and three-dimensional flows. For these problems more and more transport equations for the closure terms are used in the Reynolds models. In this way, however, the computational effort and the number of coefficients increase. Thus, the large eddy simulation method will become a promising alternative of comparable effectiveness but of much higher universality and reliability. This tendency has recently been quantified by Chapman, NASA, in considering actual trends in development of computer memory and speed [10]. He concluded, if these actual trends prevail in the next decade, the large eddy simulations will be used in the late 1990s for investigations of the flow over complete practical aircraft configurations. About the same time schedule will also hold for the advance of the large eddy simulation method towards mesoscale meteorology as the required numbers of mesh cells are quite comparable. In most other fields of technical interest applications of the method can be expected earlier because the grid requirements are usually less serious.

* Since preparation of this contribution in 1983, direct simulations of pressure driven turbulent channel flows have been performed; see e.g. the papers by Moin and Kim in *EUROMECH 199 - Direct and Large Eddy Simulation of Turbulence*, R. Friedrich, U. Schumann (Eds.), Vieweg Braunschweig (1986).

ACKNOWLEDGMENTS

I am indebted to Professor Schumann, DFVLR, for his constant interest and support. Many valuable suggestions by Dr. Homann, KfK, helped to improve the manuscript, and the comments by Dr. Sengpiel, KfK, are also gratefully acknowledged. Further thanks are due to Mrs. Oberacker for preparing the illustrations and to Mrs. Stephany for typing the manuscript.

REFERENCES

1. Orszag, S. A., and Kells, L. C., "Transition to Turbulence in Plane Poiseuille and Plane Couette Flow," *J. Fluid Mech.*, 96 (1980), p. 159–205.
2. Patera, A. T., and Orszag, S. A., "Transition and Turbulence in Planar Channel Flows," *Lecture Notes in Physics*, 141, Springer 1981, p. 329–335.
3. Kleiser, L., "Numerische Simulationen zum laminar-turbulenten Umschlagsprozeß der ebenen Poiseuille-Strömung," Dissertation, Universität Karlsruhe (1982), KfK 3271.
4. Kleiser, L., and Schumann, U., "Spectral Simulations of the Laminar-Turbulent Transition Process in Plane Poiseuille Flow," Symp. on Spectral Methods for Partial Differential Equations, Aug. 16–18, 1982, ICASE, NASA Langley Research Center, Hampton, Va., Proc. to be published by SIAM, Philadelphia, Pa.
5. McLaughlin, J. B., and Orszag, S. A., "Transition from Periodic to Chaotic Thermal Convection," *J. Fluid Mech.*, 122 (1982), p. 123–142.
6. Schumann, U., Grötzbach, G., and Kleiser, L., "Direct Numerical Simulation of Turbulence," in *Prediction Methods for Turbulent Flows*, W. Kollmann (Ed.), Hemisphere Publ. Corp. (1980), p. 123–258.
7. Orszag, S. A., and Israeli, M., "Numerical Simulation of Viscous Incompressible Flows," *Annual Rev. Fluid Mech.*, 6 (1974), p. 281–318.
8. Orszaq, S. A., "Turbulence and Transition: a Progress Report," *Lecture Notes in Physics*, 59, Springer (1976), p. 32–51.
9. Love, M. D., "An Introduction to the Large Eddy Simulation Technique," *J. Inst. Nucl. Eng.*, 20 (1979), p. 35–42.
10. Chapman, D. R., "Computational Aerodynamics; Development and Outlook," *AIAA-Journal*, 17 (1979), p. 1293–1313.
11. Ferziger, J. H., *Higher-Level Simulations of Turbulent Flows*, Stanford University, Thermosciences Division, Report TF-16, 1981.
12. Leslie, D. C., "Simulation Methods for Turbulent Flows," *Numerical Methods for Fluid Dynamics*, K. W. Morton and M. J. Baines (Eds.), Academic Press, London, 1982, p. 63–80.
13. Schumann, U., "Subgrid Scale Model for Finite Difference Simulations of Turbulent Flows in Plane Channels and Annuli," *J. Comp. Physics*, 18 (1975), p. 376–404.
14. Smagorinsky, J. S., "General Circulation Experiments with the Primitive Equations," *Mon. Weather Rev.*, 91 (1963), p. 99–164.
15. Lilly, D. K., "The Representation of Small-Scale Turbulence in Numerical Simulation Experiments," Proc. IBM Scientific Comp. Symp. on Environmental Sciences, IBM Form No. 320-1951, 1967, p. 195–210.
16. Deardorff, J. W., "A Numerical Study of Three-Dimensional Turbulent Channel Flow at Large Reynolds Numbers," *J. Fluid Mechanics*, 41 (1970), p. 453–480.
17. Deardorff, J. W., "Three-Dimensional Numerical Modeling of the Planetary Boundary Layer," Workshop in Micrometeorology, D. A. Haugen (Ed.), A.M.S. 1973, p. 271–311.
18. Schemm, C. E., and Lipps, F. B., "Some Results from a Simplified Three-Dimensional Numerical Model of Atmospheric Turbulence," *J. Atmospheric Sciences*, 33 (1976), p. 1021–1041.
19. Schumann, U., "Ein Verfahren zur direkten numerischen Simulation turbulenter Strömungen in Platten- und Ringspaltkanälen und über seine Anwendung zur Untersuchung von Turbulenzmodellen," Dissertation, Universtät Karlsruhe, 1973, KfK 1854, English translation in NASA TT T-15391.
20. Schumann, U., "Numerical Investigation of the Wall Pressure Fluctuations in Channel Flows" *Nucl. Engng. Design*, 32 (1975), p. 37–46.

21. Grötzbach, G., "Direkte numerische Simulation turbulenter Geschwindigkeits-, Druck- und Temperaturfelder bei Kanalströmungen," Dissertation, Universität Karlsruhe, 1977, KfK 2426, English translation in DOE-tr-61.
22. Grötzbach, G., "Direct Numerical Simulation of Secondary Currents in Turbulent Channel Flows," *Lecture Notes in Physics*, 76, Springer (1978), p. 308–319.
23. Leonard, A., "Energy Cascade in Large Eddy Simulations of Turbulent Fluid Flows," *Adv. in Geophysics*, 18A (1974), p. 237–248.
24. Mansour, N. N., et al., "Improved Methods for Large Eddy Simulations of Turbulence" *Turbulent Shear Flows I*, F. Durst et al. (Ed.), Springer 1979, p. 386–401.
25. Moin, P., Reynolds, W. C., and Ferziger, J. H., "Large Eddy Simulation of Incompressible Turbulent Channel Flow," Stanford University, Thermosciences Division, Report TF-12, 1978.
26. Antonopoulos-Domis, "Large-Eddy Simulation of Passive Scalar in Isotropic Turbulence," *J. Fluid Mech.*, 104 (1981), p. 55–79.
27. Champagne, F. H., "The Fine-Structure of the Turbulent Velocity Field," *J. Fluid Mech.*, 86 (1978), p. 67–108.
28. Hinze, J. O., *Turbulence*, McGraw Hill, New York, 1975, 2nd Ed.
29. Monin, A. S., and Yaglom, A. M., *Statistical Fluid Mechanics: Mechanics of Turbulence*, Vol.1 (1971); Vol. 2 (1975), MIT-Press London.
30. Lörcher, G., "Laser-Doppler-Messungen von Energiedichtespektren in Turbulenter Kanalströmung," Dissertation, Universität Karlsruhe, 1977, KfK 2448.
31. Grötzbach, G., "Numerical Simulation of Turbulent Temperature Fluctuations in Liquid Metals," *Int. J. Heat Mass Transfer*, 24, (1981), p. 475–490.
32. Herring, J. R., "Subgrid Scale Modelling—An Introduction and Overview," *Turbulent Shear Flows I*, F. Durst et al. (Ed.), Springer, 1979, p. 347–352.
33. Sommeria, G., "Three-Dimensional Simulation of Turbulent Processes in an Undisturbed Trade Wind Boundary Layer," *J. Atmospheric Sciences*, 33 (1976), p. 216–241.
34. Deissler, R. G., "Turbulent Solution of the Navier-Stokes Equations," *Phys. Fluids*, 24 (1981), p. 1595–1601.
35. Grötzbach, G., "Numerical Investigation of Radial Mixing Capabilities in Strongly Buoyancy-Influenced Vertical, Turbulent Channel Flows," *Nucl. Engng. Design*, 54 (1979), p. 49–66.
36. Cebeci, T., "A Model for Eddy Conductivity and Turbulent Prandtl Number," *J. Heat Transfer*, 95 (1973), p. 227–234.
37. Rotta, J. C., "Statistiche Theorie nichthomogener Turbulenz," *Zeitschrift für Physik*, 129 (1951), p. 547–572; 131 (1951), p. 51–77.
38. Jones, W. P., and Launder, B. E., "The Calculation of Low-Reynolds-Number Phenomena with a Two-Equation Model of Turbulence," *Int. J. Heat Mass Transfer*, 16(1973), p. 1119–1130
39. McMillan, O. J., and Ferziger, J. H., "Direct Testing of Subgrid-Scale Models," *AIAA-Journal*, 17 (1979), p. 1340–1346.
40. Uberoi, M. S., and Kovasznay, L. S. G., "On Mapping and Measurement of Random Fields," *Quart. Appl. Math.*, 10 (1952), p. 375–393.
41. Grötzbach, G., and Schumann, U., "Direct Numerical Simulation of Turbulent Velocity-, Pressure-, and Temperature-Fields in Channel Flows," *Turbulent Shear Flows I*, F. Durst et al. (Ed.), Springer, 1979, p. 370–385.
42. Moin, P., and Kim, J., "Numerical Investigation of Turbulent Channel Flow," *J. Fluid Mech.*, 118 (1982), pp. 341–377.
43. Hishida, M., and Nagano, Y., "Structure of Turbulent Velocity and Temperature Fluctuations in Fully Developed Pipe Flow," *J. Heat Transfer*, 101 (1979), p. 15–22.
44. Comte-Bellot, G., *Ecoulement Turbulent Entre Deux Parois Paralleles*, Publications Scientifiques et Techniques du Ministère de l'Air, 1965, No. 419.
45. Agrawal, A. K., and Peckover, R. S., "Nonuniform Grid Generation for Boundary-Layer Problems," *Comp. Physics Communications*, 19 (1980), p. 171–178.
46. Williams, P. G., "Numerical Integration of the Three-Dimensional Navier-Stokes Equations for Incompressible Flow," *J. Fluid Mech.*, 37 (1969), p. 727–750.
47. Forsythe, G. E., and Wasow, W. R., *Finite-Difference Methods for Partial Differential Equations*, John Wiley & Sons, New York, 1960.

48. Churchill, S. W., Chao, P., Ozoe, H., "Extrapolation of Finite-Difference Calculations of Laminar Natural Convection in Enclosures to Zero Grid Size," *Num. Heat Transfer* 4 (1981), p. 39–51.
49. Eckelmann, H., "The Structure of the Viscous Sublayer and the Adjacent Wall Region in a Turbulent Channel Flow," *J. Fluid Mech.*, 65 (1974), p. 439–459.
50. Grötzbach, G., "Spatial Resolution Requirements for Direct Numerical Simulation of the Rayleigh-Benard Convection," *J. Comp. Physics*, 49 (1983), p. 241–264.
51. Roache, P. J., *Computational Fluid Dynamics*, Hermosa Publ., Albuquerque, 2nd ed., 1976.
52. Schumann, U., "Linear Stability of Finite Difference Equations for Three-dimensional Flow Problems," *J. Comp. Physics*, 18 (1975), p. 465–470.
53. Chorin, A. J., "Numerical Solution of the Navier-Stokes Equations," *Math. Comp.*, 22 (1968), p. 745–762.
54. Amsden, A. A., and Harlow, F. H., "The SMAC Method: a Numerical Technique for Calculating Incompressible Fluid Flows," Los Alamos, 1970, LA-4370.
55. Kleiser, L., and Schumann, U., "Treatment of Incompressibility and Boundary Conditions in 3-D Numerical Spectral Simulations of Plane Channel Flows," Proc. 3rd GAMM-Conf. on Numerical Methods in Fluid Mechanics, Ed. E. H. Hirschel, Vieweg Verlag, Braunschweig, 1980, p. 165–173.
56. Buzbee, B. L., et al. "The Direct Solution of the Discrete Poisson Equation on Irregular Regions," *SIAM J. Numer. Anal.*, 8 (1971), p. 722–736.
57. Schumann, U., and Benner, J., "Direct Solution of the Discretized Poisson-Neumann Problem on a Domain Composed of Rectangles," *J. Comp. Physics*, 46 (1982), p. 1–14.
58. Grötzbach, G., "Direct Numerical Simulation of Laminar and Turbulent Bénard Convection," *J. Fluid Mech.*, 119 (1982), p. 27–53.
59. Shirani, E., Ferziger, J. H., and Reynolds, W. C., "Mixing of a Passive Scalar in Isotropic and Sheared Homogeneous turbulence," Stanford University, Thermosciences Division, Report TF-15, 1981.
60. Lipps, F. B., and Somerville, C. J., "Dynamics of Variable Wavelength in Finite-Amplitude Bénard Convection," *Phys. Fluids*, 14 (1971), p. 759–765.
61. Ozoe, H., et al., "Three-Dimensional, Numerical Analysis of Laminar Natural Convection in a Confined Fluid Heated From Below," *J. Heat Transfer*, 98 (1976), p. 202–207.
62. Lipps, F. B., "Numerical Simulation of Three-Dimensional Bénard Convection in Air," *J. Fluid Mech.*, 75 (1976), p. 113–148.
63. Hathaway, D. H., Somerville, R. C. J., "Three-Dimensional Simulations of Convection in Layers with Tilted Rotation Vectors," *J. Fluid Mech.*, 126 (1983), p. 75–89.
64. Oertel, H., Jr., "Three-Dimensional Convection within Rectangular Boxes," Natural Convection in Enclosures, K. E. Torrance and I. Catton (Eds.), ASME, HTD-Vol. 8, 1980 p. 11–16.
65. Kirchartz, K. R., Oertel, H., Jr., and Zierep, J., "Time-Dependent Convection," *Convective Transport and Instability Phenomena*, J. Zierep and H. Oertel Jr. (Eds.), Verlag Braun, Karlsruhe, 1982, p. 101–122.
66. Bühler, K., and Oertel, H., "Thermal Cellular Convection in Rotating Rectangular Boxes," *J. Fluid Mech.*, 114 (1982), p. 261–282.
67. Grötzbach, G., "Spatial Resolution Requirements for Numerical Simulation of Internally Heated Fluid Layers," *Numerical Methods in Laminar and Turbulent Flow*, C. Taylor and B. A. Schrefler (Ed.), Pineridge Press Ltd. 1981, p. 593–604.
68. Grötzbach, G., "Direct Numerical Simulation of the Turbulent Momentum and Heat Transfer in an Internally Heated Fluid Layer," *Heat Transfer*, 1982, U. Grigull, et al. (Eds.), 2, Hemisphere, 1982, p. 141–146.
69. Peskin, R. L., "Numerical Simulation of Lagrangian Turbulent Quantities in Two and Three Dimensions," *Advances in Geophysics*, 18A (1974), p. 141–163.
70. Grötzbach, G., "Convective Velocities of Wall Pressure Fluctuations in a Turbulent Channel Flow Deduced from a Computer-Generated Movie," *Lecture Notes in Physics*, 76, Springer, 1978, p. 320–324.
71. Deardorff, J. W., "The Use of Subgrid Transport Equations in a Three-Dimensional Model of Atmospheric Turbulence," *J. Fluids Engng.*, 95 (1973), p. 429–438.

72. Deardorff, J. W., "Three-Dimensional Numerical Study of the Height and Mean Structure of a Heated Planetary Boundary Layer," *Boundary-Layer Meteorology*, 7 (1974), p. 81–106.
73. Baron, F., and Laurence, D., "Large Eddy Simulations of a Wall-Bounded Turbulent Jet Flow and of Homogeneous Shear Flow," 4-th Symposium on Turbulent Shear Flows, Karlsruhe, F. R. G. (September 12–14, 1983), Proc. p. 4.7–4.12.
74. Kim, J., "The Effect of Rotation on Turbulence Structure," 4-th Symposium on Turbulent Shear Flows, Karlsruhe, F. R. G. (Steptember 12–14, 1983), Proc. p. 6.14–6.19.
75. Peckover, R. S., and Hutchinson, I. H., "Convective Rolls Driven by Internal Heat Sources," *Phys. Fluids*, 17 (1974), p. 1369–1371.
76. Emara, A. A., and Kulacki, F. A., "A Numerical Investigation of Thermal Convection in a Heat-Generating Fluid Layer," *J. Heat Transfer*, 102 (1980), p. 531–537.
77. Mayinger, F., et al., "Untersuchung thermohydraulischer Vorgänge sowie Wärmeaustausch in der Kernschmelze," Abschlußbericht BMFT-RS 48/1, Teil I, 1975.
78. Biasi, L., Castellano, L., and Holtbecker, H., *Molten Pool Theoretical Studies*, PAHR-Information Exchange, Argonne, Ill. (Nov. 2–4, 1977), ANL 78-10.
79. Steinberner, U., and Reineke, H. H., "Turbulent Buoyancy Convection Heat Transfer with Internal Heat Sources," Proc. 6th Int. Heat Transfer Conf., Toronto, 2 (1978), p. 305–310.
80. Kulacki, F. A., and Goldstein, R. J., "Thermal Convection in a horizontal Fluid Layer with Uniform Volumetric Energy Sources," *J. Fluid Mech.*, 55 (1972), p. 271–287.
81. Kulacki, F. A., and Goldstein, R. J., "Eddy Heat Transport in Thermal Convection with Volumetric Energy Sources," Proc. Fifth Int. Heat Transfer Conf., Tokyo, 3 (1974), p. 64–68.
82. Jahn, M., "Holographische Untersuchung der freien Konvektion in einer Kernschmelze," Dissertation, Techn. Universität Hannover, F. R. G., 1975.
83. Tveitereid, M., "Thermal Convection in a horizontal Fluid Layer with Internal Heat Sources," *Int. J. Heat Mass Transfer*, 21 (1978), p. 335–339.
84. Krishnamurti, R., "Finite Amplitude Convection with Changing Mean Temperature, Part 1 and 2," *J. Fluid Mech.*, 33 (1968), p. 445–463.
85. Fieg, G., "Wärmeübergangsmessungen aus intern beheizten Flüssigkeiten in zylinderförmigen Konvektionszellen," Kernforschungszentrum Karlsruhe, KfK 2712, 1978.
86. Reynolds, A. J., "The Prediction of Turbulent Prandtl and Schmidt Numbers," *Int. J. Heat Mass Transfer*, 18 (1975), p. 1055–1069.
87. Lawn, C. J., "Turbulent Temperature Fluctuations in Liquid Metals," *Int. J. Heat Mass Transfer*, 20 (1977), p. 1035–1044.
88. Jischa, M., Rieke, H. B., "About the Prediction of Turbulent Prandtl and Schmidt Numbers from Modeled Transport Equations," *Int. J. Heat Mass Transfer*, 22 (1979), p. 1547–1555.
89. Dutt, N. V. K., "Turbulent Heat Transfer Characteristics of Liquid Metals," *J. Scient. Ind. Res.*, 36 (1977), p. 165–171.
90. Grötzbach, G., "Erste Ergebnisse der direkten numerischen Simulation von Temperaturfeldern bei turbulenter Natriumströmung," Kernforschunszentrum Karlsruhe (1976), KfK 1276/2, p. 129-6–129-11.
91. Fuchs, H., "Wärmeübertragung an strömendes Natrium—Theoretische und experimentelle Untersuchungen über Temperaturprofile und turbulente Temperaturschwankungen bei Rohrgeometrie," Diss. Eidgen. Technische Hochschule Zürich, EIR-Bericht Nr. 241, Würenlingen (1973).
92. Gräber, H., "Der Wärmeübergang in glatten Rohren, zwischen parallelen Platten, in Ringspalten und Längs-Rohrbündeln bei exponentieller Wärmeflußverteilung in erzwungener laminarer oder turbulenter Strömung," *Int. J. Heat Mass Transfer*, 13 (1970), p. 1645–1703.
93. Barthels, H., "Darstellung des Wärmeübergangs in konzentrischen Ringspalten unter Benutzung der Analogie zwischen Impuls- und Wärmeaustausch," Dissertation, Technische Hochschule Aachen, Jül-506-RB, 1967.
94. Dwyer, O. E., "On the Transfer of Heat to Fluids Flowing through Pipes, Annuli, and Parallel Plates," *Nucl. Science and Engng.*, 17 (1963), p. 336–344.
95. Dwyer, O. E., Hlavac, P. J., and Nimmo, B. G., "Eddy Diffusivity of Heat Transfer in the Radial Direction for Turbulent Flow of Mercury in Annuli," *Int. J. Heat Mass Transfer*, 20 (1977), p. 141–151.

96. Bobkov, V. P., Ibragimov, M. Kh., Subbotin, V. I., "Statistische Daten über turbulente Temperaturschwankungen in der Strömung," Zhidkie metally, Moskau (1967), p. 53–71, German translation KfK-tr-372.
97. Rust, J. H., and Sesonske, A., "Turbulent Temperature Fluctuations in Mercury and Ethylene Glycol in Pipe Flow," *Int. J. Heat Mass Transfer*, 9 (1966), p. 215–227.
98. Hochreiter, L. E., and Sesonske, A., "Turbulent Structure of Isothermal and Nonisothermal Liquid Metal Pipe Flow," *Int. J. Heat Mass Transfer*, 17 (1974), p. 113–123.
99. Bunschi, J, Turbulente Temperaturschwankungen in flüssigem Natrium," Diss. Eidgen. Technische Hochschule Zürich, AF-NST-13, Würenlingen 1977, Engl. translation in ORNL-tr-4963.
100. Grötzbach, G., "Numerical Simulation of Turbulent Liquid Metal Flows in Plane Channels and annuli," Kernforschungszentrum Karlsruhe, 1980, KfK 2968.
101. Grötzbach, G., "Über das räumliche Auflösungsvermögen numerischer Simulationen von turbulenter Bénard-Konvektion," Kernforschungszentrum Karlsruhe (1980), KfK 2981 B.
102. Launder, B. E., "On the Effects of a Gravitational Field on the Turbulent Transport of Heat and Momentum," *J. Fluid Mech.* 67 (1975), p. 569–581.
103. Chen, C. J., and Rodi, W., "On Decay of Vertical Buoyant Jets in Uniform Environment," Proc. 6-th Int. Heat Transfer Conference, Toronto, (August 7–11, 1978).
104. Goldstein, R. J., "Film Cooling," *Advances in Heat Transfer*, 7, Academic Press (1971), p. 321–379.
105. Petukhov, B. S., "Turbulent Flow and Heat Transfer in Pipes under Considerable Effect of Thermogravitational Forces," Proc. Int. Seminar Turbulent Buoyant Convection, Dubrovnik 1976, Ed. D. B. Spalding, N. Afgan, Hemisphere Publ. Corp. 1977, p. 701–717.
106. Erb, E., et al., "Auslegung, Vorausberechnung und Auswertung der HDR-Blowdown-Experimente zur dynamischen Belastung und Beanspruchung von Reaktordruckbehältereinbauten," Halbjahresbericht 1978/1, Projekt Nukleare Sicherheit, KfK 2700 (1978), p. 4100/1-4100/7.

Gulf Publishing Company
Book Division
Houston, London, Paris, Tokyo

Encyclopedia of Fluid Mechanics

VOLUME 6

Complex Flow Phenomena and Modeling

N. P. Cheremisinoff, Editor

in collaboration with—

B. Abedian
S. K. Achwal
E. E. Adams
A. M. Baptista
P. N. Cheremisinoff
T. Chiba
V. H. Chu
M. Crine
J. T. Davies
M. Davis
R. G. Deissler
J. Dowden
K. M. Foreman
U. P. Ganguly
M. A. Gill
G. Grötzbach
P. H. Guldberg
P. S. Gupta
V. Guvanasen
G. L'Homme
D. W. Hubbard
K. Hutter
G. H. Jirka
P. Kapadia
T. Katayama
Y. Kato
J. M. Lee
N. C. Markatos
J. Mewis
M. Mihelcic
H. Mingmin
H. Moritomi
S. Morooka
J. D. Murphy
D. Myrhaug
T. K. O'Neill
C. P. Perdikis
C. J. S. Petrie
H. Qiwei
A. A. Raptis
J. A. Reuther
P. C. Sabatier
W. A. Shay
D. N. Smith
G. J. Stiegel
F. Sun
T. Takamatsu
R. D. Tonini
K. Ueyama
R. E. Volker
H. L. Webster
K. Wingerath
M. Yamaguchi
A. Yoshizawa

Encyclopedia of Fluid Mechanics

VOLUME 6

Complex Flow Phenomena and Modeling

Library of Congress Cataloging-in-Publication Data

(Revised for vols. 5 & 6)
Main entry under title

Encyclopedia of fluid mechanics.

Includes index.
Contents: v. 1. Flow phenomena and measurement— — v. 5. Slurry flow technology—v. 6. Complex flow phenomena and modeling.
1. Fluid mechanics—Dictionaries. I. Cheremisinoff, Nicholas P.
TA357.E53 1985 620.1'06 85-9742

ISBN 0-87201-513-0 (Vol. 1)
ISBN 0-87201-514-9 (Vol. 2)
ISBN 0-87201-515-7 (Vol. 3)
ISBN 0-87201-516-5 (Vol. 4)
ISBN 0-87201-517-3 (Vol. 5)
ISBN 0-87201-518-1 (Vol. 6)
ISBN 0-87201-540-8 (Vol. 7)
ISBN 0-87201-542-4 (Vol. 8)

ISBN 0-87201-518-1